

LA-UR-15-24681

Approved for public release; distribution is unlimited.

Title: Robust Relative Magnitude Thresholds for a Multichannel Correlation
Detector in the Presence of Background Seismicity

Author(s): Carmichael, Joshua Daniel
Hartse, Hans Edward

Intended for: Bulletin of the Seismological Society of America

Issued: 2015-06-22

Disclaimer:

Los Alamos National Laboratory, an affirmative action/equal opportunity employer, is operated by the Los Alamos National Security, LLC for the National Nuclear Security Administration of the U.S. Department of Energy under contract DE-AC52-06NA25396. By approving this article, the publisher recognizes that the U.S. Government retains nonexclusive, royalty-free license to publish or reproduce the published form of this contribution, or to allow others to do so, for U.S. Government purposes. Los Alamos National Laboratory requests that the publisher identify this article as work performed under the auspices of the U.S. Department of Energy. Los Alamos National Laboratory strongly supports academic freedom and a researcher's right to publish; as an institution, however, the Laboratory does not endorse the viewpoint of a publication or guarantee its technical correctness.

Robust Relative Magnitude Thresholds for a Multichannel Correlation Detector in the Presence of Background Seismicity

Joshua D Carmichael, Hans Hartse

June 18, 2015

Contents

1	Introduction	1
2	Organization of Paper	3
3	Background	3
4	Data	6
4.1	Threshold Magnitude Estimates for Collocated Template and Target Sources	7
4.2	Threshold Magnitude Estimates for Spatially Separated Template and Target Sources	9
5	Results	11
5.1	Collocated Explosions	11
5.2	Non-Collocated Explosions	12
6	Discussion	13
6.1	Detector Performance	13
6.2	Threshold Magnitudes	14
6.3	The DOY 132 Seismic Event	14
7	Conclusions	16
	Appendices	29
	Appendix A A Statistical Theory of Correlation Detectors: Target and Non-Target Waveforms	30
A.1	Effective Degrees of Freedom	32
A.2	Verification of the Signal-Present Density Function	33
	Appendix B Relative Magnitudes of Collocated, Similar Explosions	36

List of Figures

1	Study Region	17
2	Template Waveforms	18
3	Relative Magnitude Detection Thresholds	19
4	Correlation Detector Processing	20
5	Correlation False Detection	21
6	Prior distribution function for Non-Target Waveform Projection	22
7	Detection Thresholds	23
8	Revised, Relative Magnitude Detection Thresholds	24
9	Reciprocity-Computed Correlation Density Function Statistics	25
10	Threshold Magnitude Estimates for Target Sources Spatially Separated from Template Sources	26
11	Localized Cross Correlation Between Test Waveforms	34
12	Empirical Validation of the Signal-Present Density Function for the Correlation Statistic	35

1 Introduction

The International Monitoring System (IMS) maintains deterrence against nuclear weapon testing by ensuring that geophysical signatures of explosive events are recorded and detected with high probability [2, 14]. Agencies like the Comprehensive Test Ban Treaty Organization (CTBTO) and Norwegian Seismic Array (NORSAR) quantify the detection performance of the IMS using statistical measurements of certain phenomenology-specific detection thresholds [24, 23, 8, 27]. Seismic-specific threshold measurements, in particular, quantify the smallest magnitude that a hypothetical seismic source can have to be detectable in an observed noise environment with a prescribed probability. These thresholds are usually computed from short-term averages of signal power that are estimated from single receivers or networks and then combined with region-specific, logarithmic magnitude scales [28, 24]. Often, such estimates are also conditioned on statistics of past seismicity originating from a given target region, but preclude details of seismic waveform geometry. To more fully exploit waveform observations, monitoring operations often apply multichannel correlation detectors to identify repeated, spatially collocated events at magnitudes well below thresholds permitted by short-term power averages. These correlation detectors use “template” waveforms recorded from reference events (e.g., tamped nuclear explosions) at receiver networks to scan multiple, contemporaneous data streams for correlated signals indicative of similar emission sources [7, 18, 15, 34, 14]. Significant correlation between the detector’s template and the network’s data stream requires intra-event similarity in waveform shape, in addition to similarity between the arrival times of equivalent waveform features composing each seismogram (e.g., P_n , L_g phases). In contrast, spatially separated explosive sources generally produce decorrelated seismic signals because the same waveform features within each seismogram instead exhibit relative time lags and intra-event interference in their waveform coda. Therefore, multichannel correlation detectors are useful for identifying low-magnitude seismic events when the template and target waveforms differ only in amplitude (magnitude), but share a radiation pattern and source location. When such sources are collocated, their relative magnitudes are related by the log-ratio of their (possibly different) waveform amplitudes [30]. Therefore, magnitudes of repeating seismic events, like multiple explosions at test sites, may be measured using correlation detectors by implementing one reference waveform as a template to detect others. Further, relative magnitudes estimated from correlation are more precise when compared to alternative estimates that use magnitude differences [9, 32]. This suggests that correlation detectors can be exploited to estimate precise, relative magnitudes of repeatable seismic events at thresholds substantially lower than provided by power detectors.

Several researchers have already exploited the relationship between repeating waveform amplitudes and multichannel correlation detectors to estimate threshold magnitudes at the North Korean Test Site (NKTS). It is particularly important to establish reliable threshold magnitudes at the NKTS. This is because North Korea is the only nation to conduct known nuclear tests this century (2006, 2009 and 2013), with some researchers claiming a locally-measured (≤ 100 km) small magnitude seismic event ($m_b \sim 1.44$) as evidence for a fourth, unannounced nuclear test on day of year (DOY) 132, 2010 [39]. By comparison, Gibbons and Ringdal [16] obtained threshold magnitudes of $m_b \sim 2.6$ for 95% detection rates at MJAR, ~ 960 km from the NKTS. They obtained this estimate by sequentially burying amplitude scaled versions of the 2009 nuclear test waveform in observed noise and then processing their resultant data with the original template. Following studies focused on the NKTS used very similar methods to estimate threshold magnitudes. Schaff *et al.* [10], for instance, estimated smaller threshold magnitudes for NKTS explosions ($m_b \sim 1.15 - 1.8$) during

April and May of 2010 at a single, three-component Chinese station (MDJ, ~ 370 km away) using a 200 sec template waveform produced by the 2009 test, motivated by the claim of an unannounced North Korean test. Ford and Walter [14] then extended these analyses by forming a network-based correlation detector from several IMS array elements and MDJ, and spectrally scaling the correlation template waveform to account for the higher corner frequencies of any small magnitude, target explosions. That work suggested that no explosion at the NKTS greater than a 1 ton could go undetected in typical noise conditions during 2010 using regional receivers. In each case, these studies have also suggested that low magnitude background seismicity ($m_b < 2$) could falsely trigger their correlation detectors at thresholds required to monitor for smaller explosions. Gibbons and Ringdal [16] mitigated such false detections by co-processing their data with frequency waveform number analyses and thereby rejected all but seven of ~ 2500 false detections originating from sources located off the NKTS. Schaff *et al.* [10] also found several false detections on events during two weeks in April and May of 2010 originating from both Manchuria, China, as well as teleseismic sources. Finally, Ford and Walter suggest that low magnitude, natural seismicity likely occurs more frequently than currently documented near the NKTS, and that this seismicity could (falsely) trigger correlation detectors. Cumulatively, these efforts both show the importance for threshold monitoring at the NKTS and an additional need to place probabilistic constraints on the smallest, confidently detectable explosion there. They additionally demonstrate a need to account for low-magnitude background (non-target) seismicity that could falsely trigger a correlation detector.

To address these research needs, we combine multichannel correlation detectors with relative magnitude estimates to demonstrate a method for computing threshold magnitudes of repeatable explosions, relative to a reference event, at thresholds that account for background seismicity. Our method differs from previous work on correlation-thresholds (e.g., [14, 10]) in three primary respects. First, we provide a calibrated, probabilistic model for the correlation detection statistics that is consistent with methods developed over previous decades for continuous threshold monitoring (e.g., [24, 28, 8, 27]). Second, we use false detections triggered by waveforms originating from background seismicity to adaptively correct our probability model and thereby adjust our correlation detector's event declaration threshold. Finally, we use reciprocity to estimate how threshold magnitudes increase when the target sources become spatially separated. We then apply our method to six months of continuously recorded data at an IMS array (USRK) to estimate the smallest explosion that is detectable at or near the NKTS with a prescribed probability, over six months in 2010. In particular, our data coverage includes the aforementioned seismic event recorded on DOY 132, 2010.

2 Organization of Paper

We first provide a summarized, quantitative theory for estimating threshold magnitudes using a multichannel correlation detector (Section 3); for continuity, we compartmentalize additional theory into more detailed Appendices (A and B). Second, we present a seismic data set we assembled from nine short period elements of the IMS array, USKR (Section 4). We then summarize an algorithm for estimating relative magnitude thresholds of collocated, explosive sources at the NKTS with our detector using these data (Section 4.1). Next, we apply this method to non-collocated, explosive sources using source-receiver reciprocity (Section 4.2); in both the collocated and non-collocated cases, we account for background seismicity. Finally, we illustrate our magnitude threshold estimates over the first six months of 2010 (Section 5) and discuss our method’s implications for monitoring test sites (Section 6 and 7).

Appendix A discusses the statistics and probability of multichannel correlation detectors as applied to seismic data and demonstrates the performance of these detectors in the presence of both target and non-target waveforms. In addition, it provides an empirical verification of the assumptions used to derive the probability density functions for the sample detection statistic output from correlation detector. Appendix B demonstrates the relationship between the relative magnitudes of collocated explosions. It further provides an estimator for sources that produce similar waveforms that is unbiased by noise and utilizes parameter estimates of the correlation detector’s probability density function.

3 Background

The threshold magnitude of a multi-correlation detector depends on the estimator used to compute the magnitude of seismic events, as well as the probability distribution for the correlation detection statistic. We show in Appendix A that the probability density function for our correlation coefficient is conditional upon the template waveform, noise field, and the wavefield that is processed by the detector. In general, any digitized seismic data is representable as a matrix \mathbf{x} with a waveform component that is correlated with the template signal, a component that is decorrelated with the template, and background noise:

$$\begin{aligned}\mathbf{x} &= A\mathbf{u} + \mathbf{u}^\perp + \mathbf{n} \\ &= \mathbf{w} + \mathbf{n},\end{aligned}\tag{1}$$

as given by the projection theorem for Hilbert Spaces [35]. In Equation 1, \mathbf{u} represents a data matrix containing the digitized multichannel template waveform, A is a scalar amplitude, \mathbf{u}^\perp is the portion of the signal decorrelated with \mathbf{u} , and \mathbf{n} is noise. We call $A\mathbf{u}$ the target signal, \mathbf{u}^\perp the non-target signal, and \mathbf{w} their (deterministic) sum. If \mathbf{x} is processed with our correlation detector, it produces a detection statistic $s(\mathbf{x})$ that is given by:

$$s(\mathbf{x}) = \frac{\langle \mathbf{x}, \mathbf{u} \rangle_F}{\|\mathbf{u}\|_F \|\mathbf{x}\|_F},\tag{2}$$

where the term $\langle \mathbf{x}, \mathbf{u} \rangle_F = \text{tr}(\mathbf{x}^T \mathbf{u})$ is the Frobenius inner product, which generalizes dot products to matrices, and $\|\mathbf{x}\|_F = \sqrt{\text{tr}(\mathbf{x}^T \mathbf{x})}$ is the Frobenius norm, which generalizes vector norms to

matrices. This correlation statistic $s(\mathbf{x})$ is a random variable with a probability density function $f_k(s(\mathbf{x}); \mathcal{H}_k)$ given by (Appendix A, Equation 16):

$$f_k(s(\mathbf{x}); \mathcal{H}_k) = \text{B}\left(s^2(\mathbf{x}); \frac{1}{2}, \frac{1}{2}(N_E - 1), \lambda, \lambda^\perp\right) + \text{B}\left(-s^2(\mathbf{x}); \frac{1}{2}, \frac{1}{2}(N_E - 1), \lambda, \lambda^\perp\right),$$

where $\text{B}(t, N_1, N_2, \alpha, \beta)$ is the doubly noncentral Beta distribution function. It is evaluated at t , has N_1 and N_2 degrees of freedom, and noncentrality parameters α and β . The presence or absence of a target signal is indexed by the hypothesis \mathcal{H}_k on the data. Hypothesis \mathcal{H}_0 symbolizes that only noise is present, whereas \mathcal{H}_1 signifies that a signal is present in the data. The scalar N_E denotes the effective number of independent samples within \mathbf{x} . The first noncentrality parameter λ in Equation 16 is proportional to the “true” correlation coefficient between the waveform template and the target data, $A\mathbf{u}$. The second noncentrality parameter λ^\perp is proportional to the signal-to-noise ratio (SNR) of the waveform \mathbf{u}^\perp that is uncorrelated with the template. Appendix A, Section A.2 documents the analytical form of both parameters (Equations 13 and 15) and presents an empirical validation (Figure 12) for the signal-present form of the density function. In the present context, we focus on relating parameters of $f_1(s(\mathbf{x}); \mathcal{H}_1)$ to the relative magnitude of the sources respectively producing the template and target waveforms. To do so, we first consider the case that data \mathbf{x} is processed with our detector and contains only noise and a target waveform. This implies that $\mathbf{u}^\perp = 0$, and that the (true) body wave magnitude of the target waveform, relative to that of the template waveform, is (Appendix A, Equation 23):

$$\Delta m = \frac{1}{2} \log_{10}(A^2),$$

where subscript “b” is suppressed, and all magnitudes are assumed to be body wave magnitudes. In Appendix A, we show that the square of the maximum likelihood estimate \hat{A}^2 for the amplitude of the target waveform is proportional to λ (Equation 14):

$$\begin{aligned} \hat{A}^2 &= \text{tr}\left(\frac{\mathbf{x}^T \hat{\mathbf{u}} \hat{\mathbf{u}}^T \mathbf{x}}{\|\mathbf{u}\|_F^2}\right) \\ &= \frac{\lambda \cdot \hat{\sigma}_0^2}{\|\mathbf{u}\|_F^2}, \end{aligned}$$

where $\hat{\sigma}_0^2$ is an estimate of the (zero mean) noise variance in \mathbf{x} and is discussed further in Section 4.1. An estimate for the magnitude of the event producing this waveform is (Appendix A, Equation 29):

$$\Delta \hat{m} = \frac{1}{2} \log_{10}\left(\left|\frac{\lambda \cdot \hat{\sigma}_0^2}{\|\mathbf{u}\|_F^2} - \frac{\hat{\sigma}_0^2 N_E}{\|\mathbf{u}\|_F^2}\right|\right),$$

We now suppose that data \mathbf{x} consists of only noise and has been processed with a multichannel correlation detector that includes template waveform \mathbf{u} . This processing operation results in a correlation statistic $s(\mathbf{x})$ that follows the four-parameter density function described by Equation 16. Two of these parameters (λ and λ^\perp) are zero in the absence of signal. Our current goal is to estimate the magnitude that a *hypothetical* seismic event in the observed noise *would* have to be

143 detectable at a 0.99 detection probability. To compute this estimate, we solve a “threshold trace”
 144 equation for λ (e.g., [28]):

$$0.99 = \Pr_D \left(\hat{\eta}, \hat{\lambda}_{99}, \lambda^\perp = 0, \hat{N}_E \right) \quad (3)$$

145 where $\hat{\eta}$ is the detector’s estimated constant false-alarm on noise threshold, $\hat{\lambda}_{99}$ is the estimate for
 146 λ that provides a 0.99 detection probability, \hat{N}_E is the effective degrees of freedom estimate in the
 147 current detection window (that includes no signal), and \Pr_D is the right tail probability integral
 148 in Equation 19. The threshold magnitude in the observed noise environment, given the detector’s
 149 threshold, is then (Appendix A; Equation 4):

$$\Delta \hat{m}_{\text{thr}} | \hat{\eta} = \frac{1}{2} \log_{10} \left(\left| \frac{\hat{\lambda}_{99} \cdot \hat{\sigma}_0^2}{\|\mathbf{u}\|_F^2} - \frac{\hat{\sigma}_0^2 \hat{N}_E}{\|\mathbf{u}\|_F^2} \right| \right).$$

150 We now consider relative threshold magnitudes for seismic events producing waveforms that are only
 151 partially correlated with the detector template so that \mathbf{u}^\perp (Equation 1) is nonzero. In particular,
 152 we suppose that the true correlation between the template \mathbf{u} and the underlying waveform \mathbf{w} , in
 153 \mathbf{x} , is ρ_∞ (Appendix A; Equation 12):

$$\rho_\infty = \frac{\langle \mathbf{w}, \mathbf{u} \rangle_F}{\|\mathbf{u}\|_F \|\mathbf{w}\|_F}$$

154 In this case, the second noncentrality parameter shaping the density function for $s(\mathbf{x})$ is nonzero
 155 (Equation 17). This means that the threshold magnitude ($\Delta \hat{m}'$) of a hypothetical seismic event
 156 providing a 0.99 detection probability in the observed noise environment will be greater in value
 157 relative to the scaled-waveform case. In this case, the noncentrality parameter estimate $\hat{\lambda}'_{99}$ for λ
 158 solves:

$$0.99 = \Pr_D \left(\hat{\eta}, \hat{\lambda}'_{99}, \frac{(1 - \rho_\infty^2)}{\rho_\infty^2} \hat{\lambda}'_{99}, \hat{N}_E \right). \quad (4)$$

159 The relative threshold magnitude for a partially coherent waveform, given a detector threshold and
 160 signal-correlation value, is then estimable from Equation 29 (Appendix A) as:

$$\Delta \hat{m}'_{\text{thr}} | \hat{\eta}, \rho_\infty = \frac{1}{2} \log_{10} \left(\left| \frac{\hat{\lambda}'_{99} \rho_\infty \cdot \hat{\sigma}_0^2}{\|\mathbf{u}\|_F^2} - \frac{\hat{\sigma}_0^2 \hat{N}_E}{\|\mathbf{u}\|_F^2} \right| \right). \quad (5)$$

161 We document quantitative details of the theory summarized above in Appendices A-B.

4 Data

Explosions at the NKTS are actively monitored using several seismometers and arrays deployed within 500 km on, or near, the Korean Peninsula. These include short period borehole arrays (USKR and KSRS) that contain additional, broadband receivers and a seismo-acoustic array near the demilitarized zone (CHNAR) that comprise both seismic and infrasound sensors. Northwest China hosts additional temporary (e.g., the NECESS array) and permanent stations (MDJ) within near-regional distances of the NKTS.

USKR is a particularly quiet, ~ 4 km aperture borehole array located near the North Korean border in southeastern Russia that is included in the International Monitoring System (IMS) [17]. It consists of nine short period, vertical channel seismometers sampling at 0.025 sec intervals emplaced at 55 m depth, and one array-centered broadband sensor, also sampling at 0.025 sec intervals. USKR was certified by the Comprehensive Test Ban Treaty Organization in 2008 and recorded both of the 2009 and 2013 announced nuclear tests. The Pn and Pg phases were recorded particularly well from both events, whereas Lg and Rg are only clearly identifiable through frequency-wavenumber analysis [16]. All receivers showed excellent recording quality over the first six months of 2010 (01/01/2010 - 06/30/2010), and suffered infrequent channel or telemetry outages.

4.1 Threshold Magnitude Estimates for Collocated Template and Target Sources

We estimate time-dependent magnitude thresholds at USRK for a multichannel correlation detector using a two-iteration algorithm. In summary, this algorithm accounts for non-target waveforms produced by background seismicity that triggers our detector and objectively readjusts event declaration criteria. Using these revised thresholds, it then computes threshold magnitudes using a false-detection probability constraint. These magnitude thresholds depend on several data statistics that must be estimated from array measurements which are contaminated by diurnally variable noise and signal clutter. To account for this variability, we segmented the data discussed below into one hour records and performed all detection and parameter estimates using 24 bins per day. This segmentation implicitly assumes that the contaminating seismic noise is statistically stationary over time periods longer than one hour. To evaluate this (and other) assumptions, we compared data statistic histograms with their predicted distributions by computing curve-fitting errors (see also Appendix A figures).

This algorithm operates in four primary stages:

First, we computed hourly estimates of noise variance by excluding seismic waveforms from our data that would artificially increase and therefore bias our estimate. To remove such waveforms, we identified events by processing data from each short-period, vertical-channel element at USRK using a noise-adaptive, digital power detector (see [5, Appendix A]). This detector computes a data statistic at each point in a seismometer data stream by dividing an estimate of the sample variance within a leading data window by an estimate of the sample variance within a longer, following window i.e., the STA/LTA [1]. To account for statistically correlated background noise, we computed robust estimates for the degree-of-freedom parameters of the data statistics' F -distribution within each detection window [4]. These updated parameters enabled us to confidently estimate the signal-absent distribution function for the STA/LTA statistic and thereby dynamically adjust the detector's event declaration threshold within each window and maintain a nearly constant false-alarm probability. We set this probability to 10^{-6} using the Neyman-Pearson decision rule [21, Chapter 7]. We then removed the waveforms producing these power detections and computed the noise variance $\hat{\sigma}_0^2$ with the remaining (almost) signal free data; the 0-subscript here indicates the variance estimate is taken assuming the null hypothesis (\mathcal{H}_0) is true.

Second, we processed the original seismic data using a multichannel correlation detector. Our waveform template comprised ~ 54 sec of data and included one sec of pre-signal, P_n through P_g phases and additional p -wave coda recorded from the 2013 nuclear test (Figure 2). We scanned all short-period data recorded at USRK between 01/01/2010 until 06/01/2010 with this template at a hour-dependent threshold that we computed from a 10^{-8} false alarm on noise constraint (equivalent to 0.03 predicted false alarms per day). Our processing included hourly estimation of the degree of freedom parameter N_E shaping the correlation statistic's null distribution $f_0(s; \mathcal{H}_0)$ and RMS errors between the correlation statistic's histogram and $f_0(s; \mathcal{H}_0)$. Any relative errors exceeding 8% were considered unreliable and omitted from further analyses. We considered any detection in the remaining data as a false alarm and saved the falsely detected waveforms. This routine resulted in 779 detected, non-target waveforms that were attributed to background seismicity (Figure 3). Our manual inspection showed that these waveforms were partially coherent with the detector's

template and thereby triggered our detector near its threshold (Figures 4-5); this threshold was often less than 0.1, as determined by the null distribution and false alarm constraint. We then computed an additional parameter λ^\perp from these triggering waveforms, which was proportional to the SNR of the template-incoherent portion of the signals.

Next, we binned our estimates for λ^\perp over the total six-month study period and thereby formed its empirical density function (histogram), $f_{\Lambda^\perp}(\lambda^\perp)$ (Figure 6). After spline-smoothing the distributional curve of $f_{\Lambda^\perp}(\lambda^\perp)$, we formed a revised null distribution for the sample correlation from the normalized product of $f_0(s|\lambda^\perp; \mathcal{H}_0)$ and $f_{\Lambda^\perp}(\lambda^\perp)$. We then integrated this conditional distribution over λ^\perp :

$$f_0(s; \mathcal{H}_0) = C \cdot \int_{\eta}^{\infty} f_0(s|\lambda^\perp; \mathcal{H}_0) f_{\Lambda^\perp}(\lambda^\perp) d\lambda^\perp \quad (6)$$

and thereby adjusted the correlation's null distribution to include influences from background seismicity (C is a normalization constant). Using the resulting unconditional density function, we computed an updated correlation detector threshold $\hat{\eta}$ that was consistent with our original 10^{-8} false alarm rate; this computation generally elevated correlation detector thresholds over their former values (Figure 7).

Last, we used our parameter estimates (e.g., $\hat{\sigma}_0^2$, \hat{N}_E , and $\hat{\eta}$) and template signal \mathbf{u} to construct hour specific, signal-present, right-tail cumulative probability functions (CDFs) for the correlation statistic. In the presence of both target and non-target waveforms, each CDF required full parametrization by a scalar λ proportional to the target waveform SNR, and a second scalar representing the template-incoherent portion of the data-stream signal energy, λ^\perp , as discussed above. Both λ and λ^\perp are functionally dependent on the mismatch correlation coefficient ρ_∞ that parameterizes potential dissimilarity between the underlying (noise-free) signals of the target and template waveforms (Appendix A; Equation 12). In the presence amplitude-scaled target waveforms without interfering signals, $\rho_\infty = 1$ so that $\lambda^\perp = 0$ (Equation 17). In this case, the threshold parameter λ consistent with a 0.99 detection probability and target-template signal correlation then minimized the functional given by:

$$\hat{\lambda}_{99} = \underset{\lambda}{\operatorname{argmin}} \left\{ \left| 0.99 - \operatorname{Pr}_D \left(\hat{\eta}, \lambda, \lambda^\perp = 0, \hat{N}_E \right) \right| \right\} \quad (7)$$

where $\lambda = \frac{\|\mathbf{w}\|^2}{\sigma_0^2}$ and $\operatorname{Pr}_D \left(\eta, \lambda, \lambda^\perp = 0, \hat{N}_E \right)$ denotes the right-tail cumulative probability distribution function for the correlation statistic under the target signal-present hypothesis, as defined by Equation 19. The estimator that gives the threshold magnitude for a target waveform consistent with an event declaration threshold $\hat{\eta}$ and detection probability Pr_D is then (Appendix A; Equation 29):

$$\Delta \hat{m} | \hat{\eta} = \frac{1}{2} \log_{10} \left(\left| \frac{\hat{\lambda}_{99} \cdot \hat{\sigma}_0^2}{\|\mathbf{u}\|_F^2} - \frac{\hat{\sigma}_0^2 \hat{N}_E}{\|\mathbf{u}\|_F^2} \right| \right).$$

We reemphasize that this estimate is conditioned upon hourly-updated, revised thresholds $\hat{\eta}$ that were adapted to mitigate false detections from background seismicity and assumes that the template and target waveform sources are collocated.

4.2 Threshold Magnitude Estimates for Spatially Separated Template and Target Sources

Our estimate for threshold magnitudes (Equation 4) are inapplicable if template and target signals become decorrelated ($\rho_\infty < 1$). Physically, such decorrelation occurs for several reasons. First, seismic signals from non-target sources (like teleseismic earthquakes) may be recorded concurrently with target signals so that the waveforms temporally interfere. Second, the size of the template and target explosive sources can be sufficiently dissimilar so that the corner frequency of the source-time function spectra do not overlap within the analysis passband [30, 14]. Third, the template and target explosive sources may be spatially separated so that the comparative, resultant waveforms show slight misalignment of equivalent seismogram features that degrades their peak cross-correlation. Quantitatively, each source of decorrelation reduces ρ_∞ and λ , but increases λ^\perp . However, these source of decorrelation are not discernible and therefore distinct sources of correlation loss can produce identical detection statistics.

To quantify the effects of correlation loss on magnitude thresholds, we specifically consider hypocentral differences of explosive sources at the NKTS. Our limited test records (2013) prevented a direct analysis of distributed source locations; such analysis requires records of identical explosions measured at range of distances from the template waveform’s source. We instead applied the principle of reciprocity between the USRK array and the NKTS to estimate decorrelation effects caused by target-template source separation, at a single receiver. The principle of reciprocity states that L receivers measure the same seismograms triggered by one source (e.g., the 2013 test) as a virtual receiver collocated with the true source would measure from L virtual sources, with the same spatial distribution as the true receivers [22]. We applied this principle to our data to estimate how target waveforms produced by sources at spatially separated USRK elements would cross-correlate at a single receiver collocated with the 2013 test hypocenter. Specifically, we computed the correlation $\rho_\infty^{(k,l)}$ between a “template” signal recording a virtual source located at receiver k against a “target” waveform triggered by a virtual source located at receiver l , where the virtual receiver was emplaced at the 2013 test location and $k, l = 1, \dots, 9$. This provided single-channel correlation estimates $\hat{\rho}_\infty$ for ρ_∞ (Figure 9; pale markers, top) that were slightly biased by noise due to the finite SNR of the waveforms. To check for consistency, we then repeated this process using waveforms triggered by the 2009 announced test (Figure 9; dark markers, top), which showed the same trend in correlation loss, despite the greater noise bias. We therefore consider our results qualitatively consistent and representative of lower bounds on true ρ_∞ estimates.

To use our estimates of ρ_∞ to compute the relative magnitude detection thresholds for a nine-element array, we first evaluated two assumptions. First, we determined if single, virtual-receiver peak correlation was sufficiently uniform across an array the size of USRK so that ρ_∞ represented the expected, multichannel value. We tested this first assumption by processing waveforms recording the 2009 test with a detector that included only single-channels of our template (single matrix columns of \mathbf{u}), and then with the full, nine-channel template. This exercise produced single-channel correlation coefficients that varied from the (full) multichannel value of 0.88 by $\leq 3\%$ over the array, and whose mean varied from full-value by less than $\leq 0.3\%$. We concluded that ρ_∞ at one receiver likely represented an array based (multichannel) correlation value.

Second, we evaluated if the parameterization of the correlation statistic’s signal-present distri-

304 bution function $f_1(s; \mathcal{H}_1)$ (Equation 16) could be extrapolated from one to nine virtual receivers.
 305 We thereby examined how \hat{N}_E changed with number of array stations recording target data. To
 306 do so, we estimated N_E using 36 virtual sub-arrays by first removing all combinations of waveform
 307 channels (matrix columns of \mathbf{u}) from our original template and then processing the data recorded
 308 over DOY 132, 2010 with each resultant template (see Equation 20 and preceding explanatory
 309 text). Next, we computed a linear fit to these estimates and extrapolated a one-station N_E es-
 310 timate to all nine stations, denoted \hat{N}'_E (Figure 9, bottom). This processing showed that while
 311 the extrapolated values were highly variable (blue bars), the linear fit (red dashed line) provided
 312 an excellent representation to the mean \hat{N}'_E values (black curve). We concluded that \hat{N}_E values
 313 estimated at a single virtual receiver could be extended to nine virtual receivers with the same
 314 spatial distribution as USRK using our linear regression. To then re-estimate threshold magnitudes
 315 for non collocated sources producing dissimilar waveforms, we combined these estimates for \hat{N}_E
 316 and ρ_∞ with Equations 4 and 7 :

$$\begin{aligned}
 \hat{\lambda}'_{99}|\hat{\rho}_\infty &= \underset{\lambda}{\operatorname{argmin}} \left\{ \left| 0.99 - \operatorname{Pr}_D \left(\hat{\eta}, \lambda, \frac{(1 - \hat{\rho}_\infty^2)}{\hat{\rho}_\infty^2} \lambda, \hat{N}'_E \right) \right| \right\} \\
 \Delta \hat{m}'|\hat{\eta}, \hat{\rho}_\infty &= \frac{1}{2} \log_{10} \left(\left| \frac{\hat{\lambda}'_{99}|\hat{\rho}_\infty \cdot \hat{\sigma}_0^2}{\|\mathbf{u}\|_F^2} - \frac{\hat{\sigma}_0^2 \hat{N}'_E}{\|\mathbf{u}\|_F^2} \right| \right).
 \end{aligned} \tag{8}$$

317 Figure 10 illustrates our threshold estimates computed from Equation 8 for DOY 132, 2010.

5 Results

5.1 Collocated Explosions

Figure 3 illustrates hourly estimates of threshold magnitudes computed over the first six months of 2010 by processing data at USRK with a 54 second Pn-Pg template (Figure 2, purple waveforms), at a detector threshold set from a 10^{-8} false alarm on-noise probability constraint (Figure 3, blue markers). This exercise predicts that seismic events ~ 3.6 magnitude units below that of the 2013 DPRK test, on average, are detectable at a 0.99 probability during the first six months of 2010 (blue markers). However, this initial estimate resulted in 779 false detections on non-target waveforms (red time series), assuming no unannounced nuclear tests took place between January and July of 2010 that were collocated with the 2013 test (see [14] versus [39]). These falsely detected waveforms triggered our correlation detector near it's threshold for event declaration and appeared to originate from background seismicity that was partially coherent with the template (e.g., Figures 4-5), but unrelated to test-site activity. Figure 6 shows the spline-smoothed empirical distribution $f_{\Lambda^\perp}(\lambda^\perp)$ (histogram) of the noncentrality parameter λ^\perp computed from the waveforms that produced these false detections. The non-uniform concentration of this distribution towards relatively low values of λ^\perp demonstrates that, on average, more false detections are induced by lower-energy rather than high-energy background seismicity. Using mean estimates for template-sample lengths (accounting for channel outages) and λ^\perp , we estimate that most background seismicity that falsely triggered our detector had an effective SNR value of at most ~ 0.6 (if $\rho_\infty = 0$). Such seismicity would not be screened using an incoherent power (STA/LTA) detector.

Figure 7 illustrates the revised thresholds that we computed from the prior distribution for λ^\perp (Figure 6) and the general correlation statistic's density function (Equation 16) using Equation 6. These revised values for η (red) for our detector's threshold uniformly increased in value and variability over their original values (blue) and more than doubled in most cases. Our manual inspection revealed that some of this variability was attributable to temporary receiver outages (USB4, 04/26) and intense microseisms which appeared to occasionally generate spectral energy above the 1.5 Hz lower cutoff of our bandpass filter. Other outliers appear driven by the presence of unusually high-energy and emergent background seismic energy that did not trigger our power detector, and thereby inflated our estimates for background noise variance $\hat{\sigma}_0^2$. Despite these influences, the theoretical density function for the correlation statistic $s(\mathbf{x})$ matched the observed statistic histogram within 8% relative error except during a few isolated hours (gray bars, Figure 7).

Revised hourly estimates of threshold magnitudes computed from the conditional η -values show uniform decrease in value and increase in variability (Figure 8) corresponding to threshold increases for the same 10^{-8} false alarm on-noise probability constraint (Figure 3, blue markers). These updated thresholds suggest that seismic events ~ 3.35 magnitude units below that of the 2013 DPRK test are detectable at a 0.99 probability and result in no false detections between 01/2010 and 06/2010 (red horizontal curve). Using a reported magnitude of 5.1 units for the 2013 test [38], this suggest explosive events collocated with the 2013 announced nuclear test can be confidently detected at USRK down to magnitudes of > 1.66 in similar emplacement conditions. Threshold magnitudes are even lower on DOY 132 during the suggested unannounced May test ([39]) and imply even small explosions are detectable at that time, where $m_b \sim 1.6$. If we use our initial detection thresholds, we estimate a relative magnitude detection threshold of $m_b \sim 1.44$. Coincidentally, this is also

the reported magnitude of the recorded event. Due to the high uncertainty of magnitude-to-yield relationships below a 0.5 kiloton at the NKTS, we do not make an equivalent yield estimate as performed by Zhang and Wen [39]

5.2 Non-Collocated Explosions

We additionally estimated threshold magnitudes for DOY 132 in cases that the correlation detector’s template waveform was not collocated with a target source waveform by invoking source-receiver reciprocity. Our validation analyses (Section 4.2) demonstrate that waveforms triggered by virtual sources located at the true USRK array elements and measured at a single NKTS-localized virtual receiver exhibit cross-correlation values that degrade quickly with source-separation distance (Figure 9; top). We further determined that the density function that describes the detection performance at this virtual receiver could be adapted to nine receivers by parameterizing the density function with an extrapolated effective-degree of freedom estimate \hat{N}_E' (Figure 9; bottom). Cumulatively, we conclude that our threshold estimation method is applicable to spatially-separated explosive sources (Equations 8). Further, we conclude that waveforms triggered by explosive sources spatially separated from a template (reference) source exhibit a higher threshold for detection using a correlation detector than do comparable, collocated sources. In particular, the peak correlation values computed from nine, spatially separated virtual sources located at USRK and measured by a single virtual receiver at the NKTS, using reciprocity, decrease from 0.65 to 0.18 correlation units over less than 3.5 km (Figure 10). Therefore, our initial estimates suggest that waveforms from these spatially separated sources must be a full magnitude unit larger to provide the same likelihood of detection when compared to collocated explosions.

Our Δm_{thr} estimates almost certainly underestimate the true thresholds since our computations were conditioned upon negatively biased $\hat{\rho}_\infty$ values. Additionally, it is unclear how these estimates transfer from the virtual USRK array location, to the dominantly granite environment of the NKTS. The peak waveform correlation between the 2009 and 2013 tests further indicates that values in Figure 10 underestimate those for the NKTS, e.g., that our threshold estimates are not directly transferable to the test site. In this case, a source-separation distance of ~ 570 m [39]) corresponds to signal-correlation of $\rho_\infty \geq 0.88$. This intra-event waveform correlation is consistent with a relative threshold magnitude of $\Delta m_{\text{thr}} = -3.37$, or an absolute threshold of $m_{\text{thr}} \sim 1.7$. In contrast, Figure 9 (top) shows that the cross-correlation between virtual sources with a similar separation is probably $\rho_\infty \leq 0.6$, indicative to a higher magnitude threshold.

To address this discrepancy, we compared correlation loss with distance at the NKTS with our vir-

tual source array at USRK. Following Menke [25], we fit an exponential model $s_{ij}(\mathbf{x}) = \exp\left(-\frac{\|\mathbf{r}_i - \mathbf{r}_j\|}{c}\right)$

relating the sample correlation $s_{ij}(\mathbf{x})$ between waveforms triggered by two spatially separated sources with separation distance $\|\mathbf{r}_i - \mathbf{r}_j\|$, using measurements from Figure 10 (c is a proportionality length). We thereby estimated a least-squares value of $\hat{c} = 1875$ m and an effective correlation distance of ~ 240 m that is consistent with an observed 2009-to-2013 waveform correlation coefficient of 0.88. This ratio suggests that spatially separated explosions at the NKTS can correlate as well as virtual sources at USRK at $2.4\times$ greater separation distances. We therefore consider the threshold estimates in Figure 10 for virtual, spatially-separated sources as lower bounds for detecting true

404 explosions at NKTS when the template and target waveform sources are not collocated.

405 6 Discussion

406 Our results have important implications for both the performance of multichannel correlation de-
407 tectors in cluttered signal environments, and more practically, for monitoring the test sites for low
408 magnitude explosions.

409 6.1 Detector Performance

410 We first consider the performance of our multichannel correlation detector. In particular, this de-
411 tector produced frequent false detections ($> 4 \text{ day}^{-1}$) despite its *predicted* 10^{-8} false-alarm-on-
412 noise probability constraint, which instead implied a false alarm rate of 0.03 events per day (see
413 calculation in [34]). Such discrepancies generally occur because correlation detectors effectively
414 test between two competing hypotheses: either a noisy target signal is present, or only noise is
415 present. In our case, low energy background seismicity ($\text{SNR} \sim 0.6$, on average) that could not
416 be identified with a power detector produced waveforms that were partially coherent with our de-
417 tector’s waveform template and thereby produced a detection statistic that exceeded our naively
418 estimated threshold. The timing of this seismicity then led to a nearly constant false detection
419 rate, which we then quantified probabilistically by modifying the correlation statistic’s probability
420 density function. This modification then allowed us to estimate revised thresholds that accounted
421 for these false detections. Even if there had been a target explosion conducted during our study
422 period among the 779 false triggers, this event would likely have not effected the revised threshold
423 values. Therefore, our method can be applied to time periods when tests at the NKTS have or
424 will occur. We further suggest that such a method may mitigate false alarms in other monitoring
425 applications and in the absence of more physically realistic hypothesis tests (e.g., [4, Section A.11]).

426
427 While these broad implications hold qualitatively, the quantitative details of our results are condi-
428 tioned on the duration and bandwidth of the pre-processed template waveform shown in Figure 2
429 (purple traces) and employed by our correlation detector. Our 54 sec template is much shorter than
430 the 200 sec waveform segment that Schaff *et al.* [10] used at MDJ to obtain lower magnitude thresh-
431 olds ($m_b \leq 1.8$). We likely would have obtained greater *predicted* performance with longer templates
432 at USRK by extending our template to include portions of L_g . We instead selected our data to only
433 include p -waves since it is unclear if explosions substantially smaller than the 2013 NKTS explosion
434 (e.g., ≥ 3 magnitude units smaller) or with different effective emplacement conditions radiate sim-
435 ilar fractions of shear wave energy [36, 26]. In contrast, p -wave segments are expected to exhibit
436 greater waveform similarity over a range of magnitudes, with their comparability limited by the
437 spectral scaling and therefore corner frequencies of the source time function [14, 11, 12]. Therefore,
438 a longer template waveform that includes shear wave segments may actually reduce the ability of
439 our correlation detector to identify smaller explosion sources at the NKTS.

6.2 Threshold Magnitudes

Our modified threshold estimates show that repeatable explosions at the NKTS can be detected with no false detections on background seismicity, at low threshold magnitudes ($m_b > 1.7$), and with very high probability (0.99% chance). We concede that our threshold estimates for collocated sources are subject to certain assumptions, however. Strictly speaking, our maximum likelihood correlation detector tests for waveforms that share spectral content with the template and are produced by a single point explosion that is collocated with the template source. We also assume that the relative amplitude scaling between a potential explosion waveform and the template is the same at all receivers. A “beamed” correlation detector that stacks single channel correlograms and used by others [14, 16] allows for different amplitude scaling at different receivers. Such a detector produces a higher detection performance in theory [3], and may therefore detect lower SNR waveforms. However, it also could lead to more frequent misidentification.

Despite these concessions, our analysis of spatially separated explosions is likely very conservative. Specifically, it provides lower bounds on the true correlation detector performance, i.e., smaller explosions at greater distances are likely more detectable than what is shown in Figure 10. This is because the reciprocity approach we employed to estimate the influence of target-template source separation provided threshold estimates for sources collocated with the USRK array, not at the NKTS. However, correlation of our template against data records from the 2009 test indicate that correlation detection provides a larger detection statistic than predicted by reciprocity. Physically, we suggest that the 2009 test’s over-buried depth, in addition to scattering and attenuation in the hard rock at the NKTS, improves repeatability of waveforms generated by proximal explosions, relative to what is expected for virtual sources at USRK.

Finally, the quantitative theory we’ve developed here for decorrelated waveforms is also applicable to monitoring scenario whereby the underlying signal of a waveform is imperfectly correlated with the detector template. In particular, if an explosion is conducted in emplacement conditions that differ from the test conditions producing the template waveform, it will generally produce signals (even without noise) that do not perfectly match with the template. In these cases, the correlation coefficient between the respective waveforms will be degraded relative to the ideal case. The relative threshold magnitude for correct identification, however, is still estimable using Equation 8. This also means that distinct sources of correlation loss between two waveforms cannot be distinguished our this method.

6.3 The DOY 132 Seismic Event

The seismic event recorded on DOY 132, 2010 and suggested by Zhang and Wen to be explosive in origin [39] was not detected at USRK with and without a false-detection modified threshold. Specifically, no seismic event near the expected arrival time at USRK was detected among the 779 false detections before probabilistically correcting the detector’s threshold for background seismicity (Figure 3). At this time, we estimate that our relative magnitude threshold was $m_{\text{thr}} \sim 1.44$, which is coincidentally the magnitude Zhang and Wen reported. Our non-detection is also consistent with earlier work [14] and suggests that the waveform triggered by the event was insufficiently similar with our explosion template to indicate a match, even at the very liberal thresholds afforded by our

⁴⁸² 10^{-8} false-alarm-on-noise probability constraint.

7 Conclusions

We develop a robust methodology for computing relative threshold magnitudes for repeating seismic events in the presence of noise and background seismicity. Our method exploits both the ability of multichannel correlation detectors to identify template similar, sub-unit SNR waveforms as well as the precision of correlation-based relative magnitude estimators. Further, we show that detector thresholds can be empirically modified to account for false-alarms triggered by non-target waveforms. Applied to the NKTS, we conclude that $m_b \geq 1.66$ magnitude-equivalent explosions collocated with the 2013 announced test can be identified ($> 99\%$ chance) at USRK using a multichannel correlation detector that operates with P -phase template waveforms and triggers zero false detections over six months. Sources located off site are more difficult to detect at the same threshold, but are still low relative to power detectors (e.g., [24]). Our estimates indicate that single-point underground explosions that produce seismic magnitudes between 2.4 and 2.7 units separated ~ 4 km from 2013 test are detectable with the at least the same 0.99 probability, but are likely very conservative. In particular, these threshold values are higher than expected from waveform correlation between the 2009 and 2013 test waveforms. A crude scaling argument instead indicates that explosions of identical magnitudes may be detected with the same 0.99 probability at 9.6 km (2.4×4 km) from the 2013 test hypocenter. We therefore suggest that reciprocity-based estimates for magnitude thresholds of spatially separated target sources are lower due to the differences in geological structure and receiver-depths at USRK, relative to structure and testing depths at the NKTS. In addition, the correlation statistic and decision rule we implement (Equation 10) is restrictive compared to correlogram beaming commonly used elsewhere (e.g., [14, 15]) but more realistically assumes similar radiation patterns between explosive sources and requires uniform amplitude scaling between different array channels. Finally, we suggest that our estimates could also be improved by including additional data from other IMS or regional stations (e.g., MDJ), which would certainly decrease the magnitude threshold at which a detection could be made.

For future work, we suggest that correlation thresholds can be further reduced by cataloging sources of low magnitude seismicity proximal to the NKTS. The addition of these events to a waveform database could then be used to construct a so-called interference subspace, whereby waveforms similar to already-cataloged events that originate from natural source or mining activity are rejected if they match previously detected, similar waveforms [33, 20]. Our continuing work includes quantifying the influence of such nuisance seismicity on alternative detectors to improve the applicability of relative magnitude threshold monitoring to more seismically active test sites.

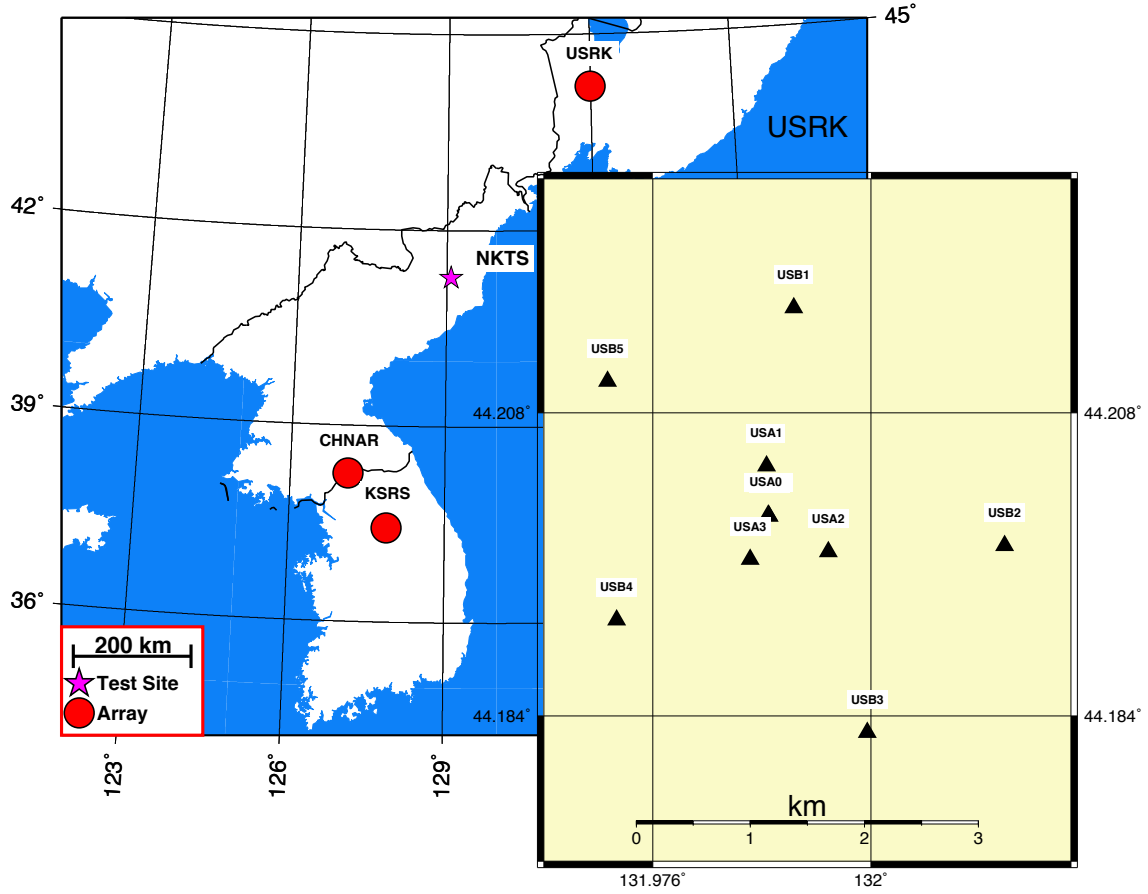


Figure 1: Seismic arrays deployed within ~ 450 km of the DPRK nuclear test site. USRK (right) consists of nine vertical channel, borehole short period sensors, and a three-component broadband receiver at the array center. Only the short-period data were used here.

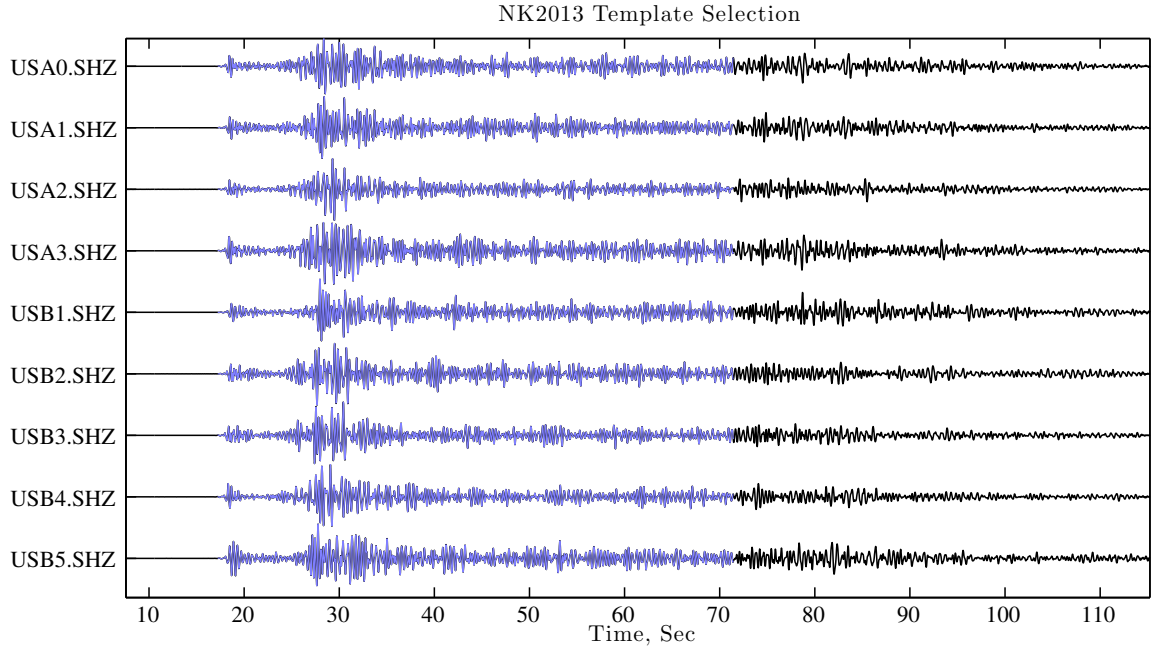


Figure 2: Vertical component seismic seismograms of the 2013 announced nuclear test (black) recorded at the short-period elements of URSK. The purple waveforms show one sec of pre-event signal, followed by 54 seconds of Pn-Pg and P waveform coda used as a waveform template. Data were detrended, bandpass filtered between 1.5 and 7.5 Hz, and Hamming tapered to mitigate spectral leakage.

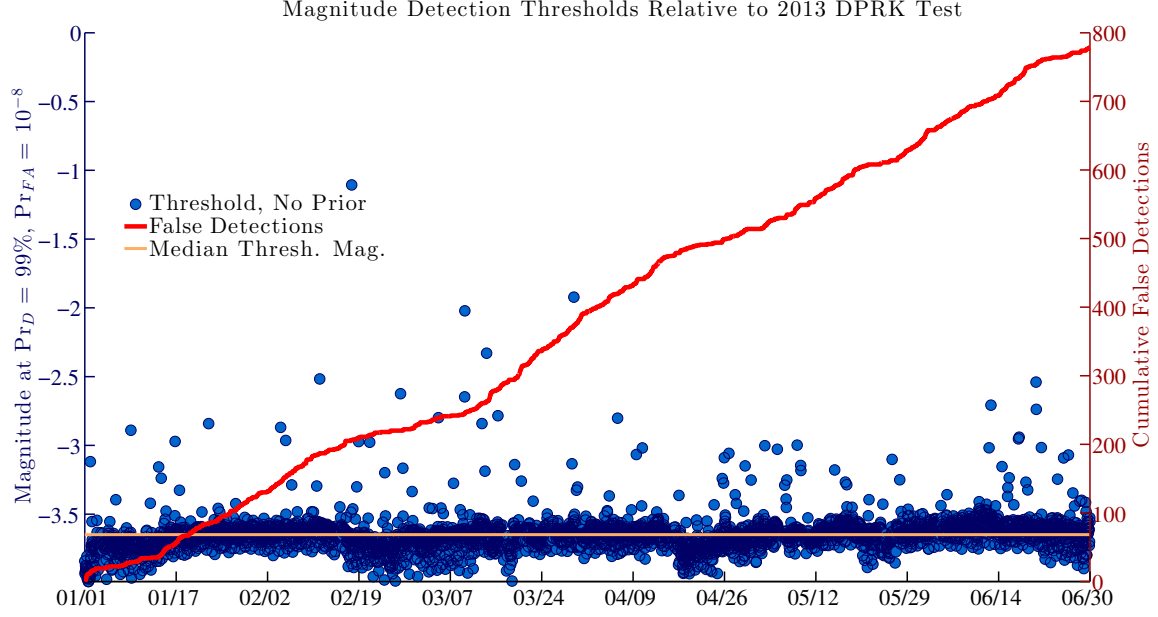


Figure 3: Relative magnitude detection thresholds without parametrization for background seismicity. Blue markers show hourly estimates of the magnitude for a hypothetical seismic event that is detectable with a 0.99 detection probability, relative to that of the NK 2013 test. The red curve illustrates the cumulative number of false detections over the six month period obtained using a detector threshold with the template from Figure 2 established by a 10^{-8} false alarm probability. The horizontal orange line shows the median threshold value. Spuriously high magnitude threshold values often coincided with channel outages, background seismicity, or narrowband noise.

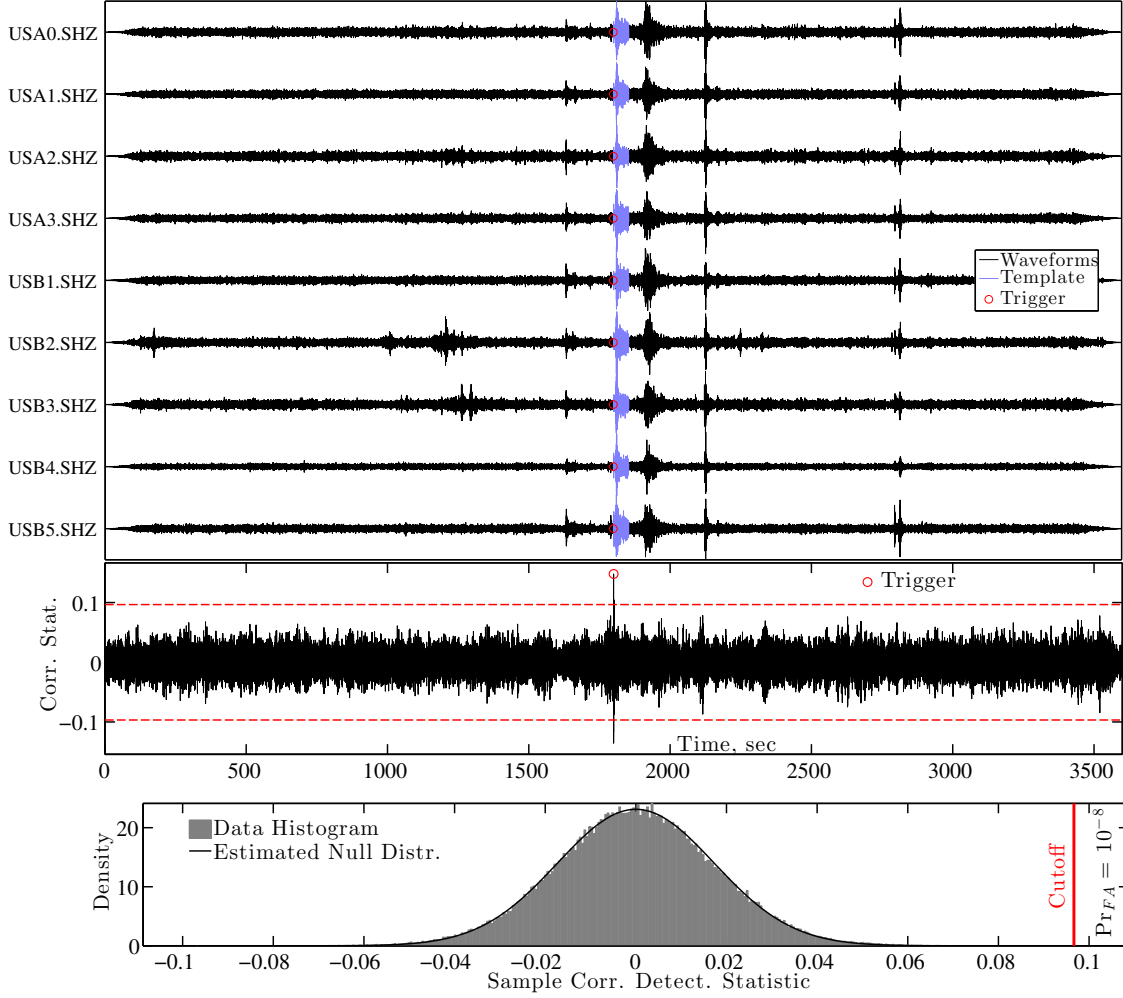


Figure 4: An example of processing data recorded at USRK in 2010 with a correlation detector that includes the template shown in Figure 2 and results in a false detection. **Top:** A nine-channel data stream (black) recorded between 05:00 and 06:00 UTC of 11, January 2010. The purple data segment shows the template waveforms superimposed on the black data-stream and temporally aligned at the peak correlation value. The red markers indicate the time of an event-declaration. **Middle:** The correlation statistic $s(\mathbf{x})$ computed by scanning the template waveform template against the data stream at top. The red, horizontal line indicates the threshold for event declaration, determined by a 10^{-8} false-alarm on noise probability constraint, as computed from the signal-absent distribution using the Neyman Pearson criteria (see histogram below). **Bottom:** The histogram computed from the correlation statistic time series (gray) superimposed with the theoretical null distribution (black curve) shaped by an effective degrees of freedom parameter \tilde{N}_E . The red vertical line shows the threshold for event declaration, consistent with a right-tail 10^{-8} probability as computed from the black curve. The theoretical distribution fits the observed histogram with a $\sim 4\%$ relative error.

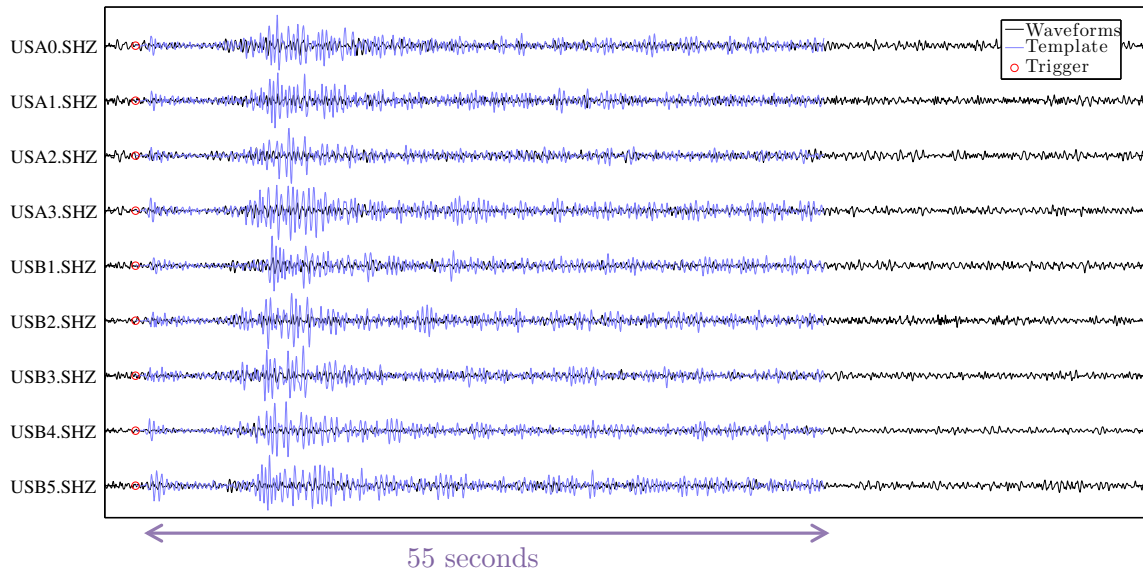


Figure 5: The non-target waveforms (black) detected on 11-Jan-2010 05:51:36 (UTC) and shown in Figure 4 superimposed with the template waveforms (purple). The detected waveforms appear partially coherent with the Pn/Pg template but are ostensibly triggered by a regional-distance earthquake.

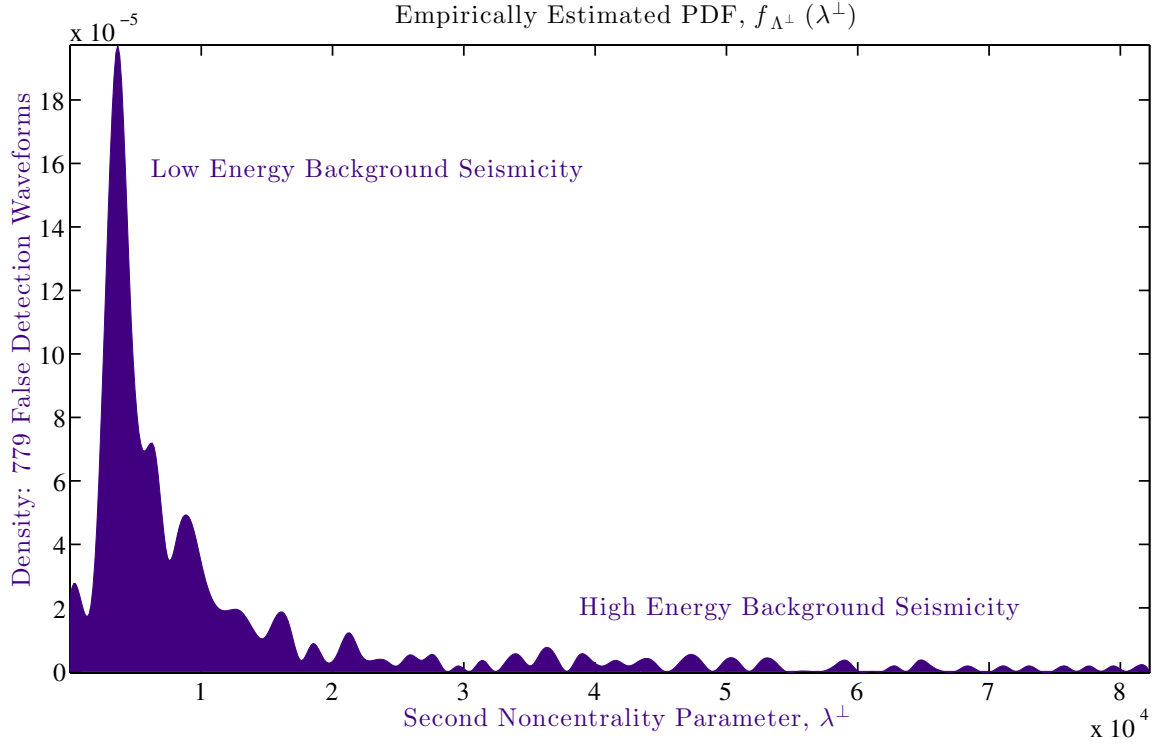


Figure 6: The spline-smoothed empirical probability density function (labeled PDF) computed for λ^\perp from the background seismic wavefield. The waveforms used to compute λ^\perp were detected using template waveforms of the DPRK 2013 nuclear test, as recorded at URSK, and correspond to the red markers in Figure 3.

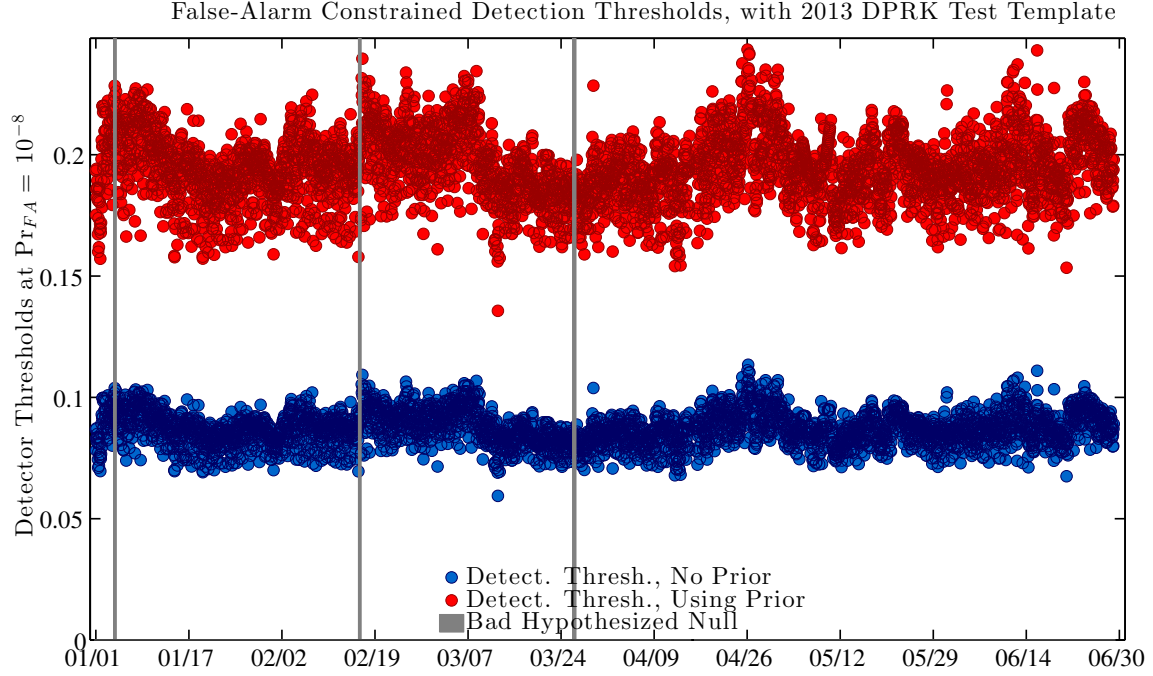


Figure 7: Thresholds for event declaration with and without accounting for background seismicity. Blue markers show the original thresholds η for event declaration, as determined by Equation 18 and assuming only signal-free background noise. Red markers show the revised detection thresholds η' computed from Equation 6. The gray vertical bars illustrate where the revised null distribution fit the correlation statistic histogram with an error of greater than 8% and we consider the coincident threshold values less reliable.

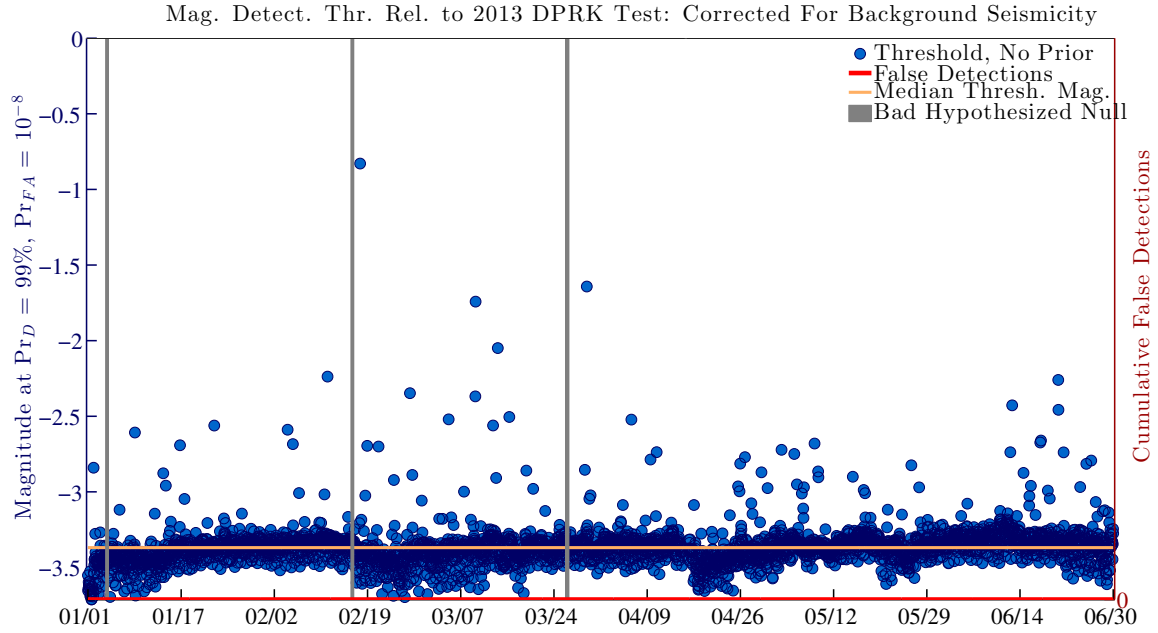


Figure 8: Relative magnitude detection thresholds including parametrization for background seismicity with revised thresholds. Blue markers show hourly estimates for the magnitude of a hypothetical seismic event that is detectable with a 0.99 detection probability, relative to that of the DPRK 2013 test (compare to Figure 3). The horizontal red curve at bottom illustrates zero cumulative number of false detections over the six month period obtained using the revised detector threshold with the template from Figure 2 established by a 10^{-8} false alarm probability. The horizontal orange line shows the median threshold value. Again, spuriously high magnitude threshold values often coincided with channel outages, background seismicity, or narrowband noise.

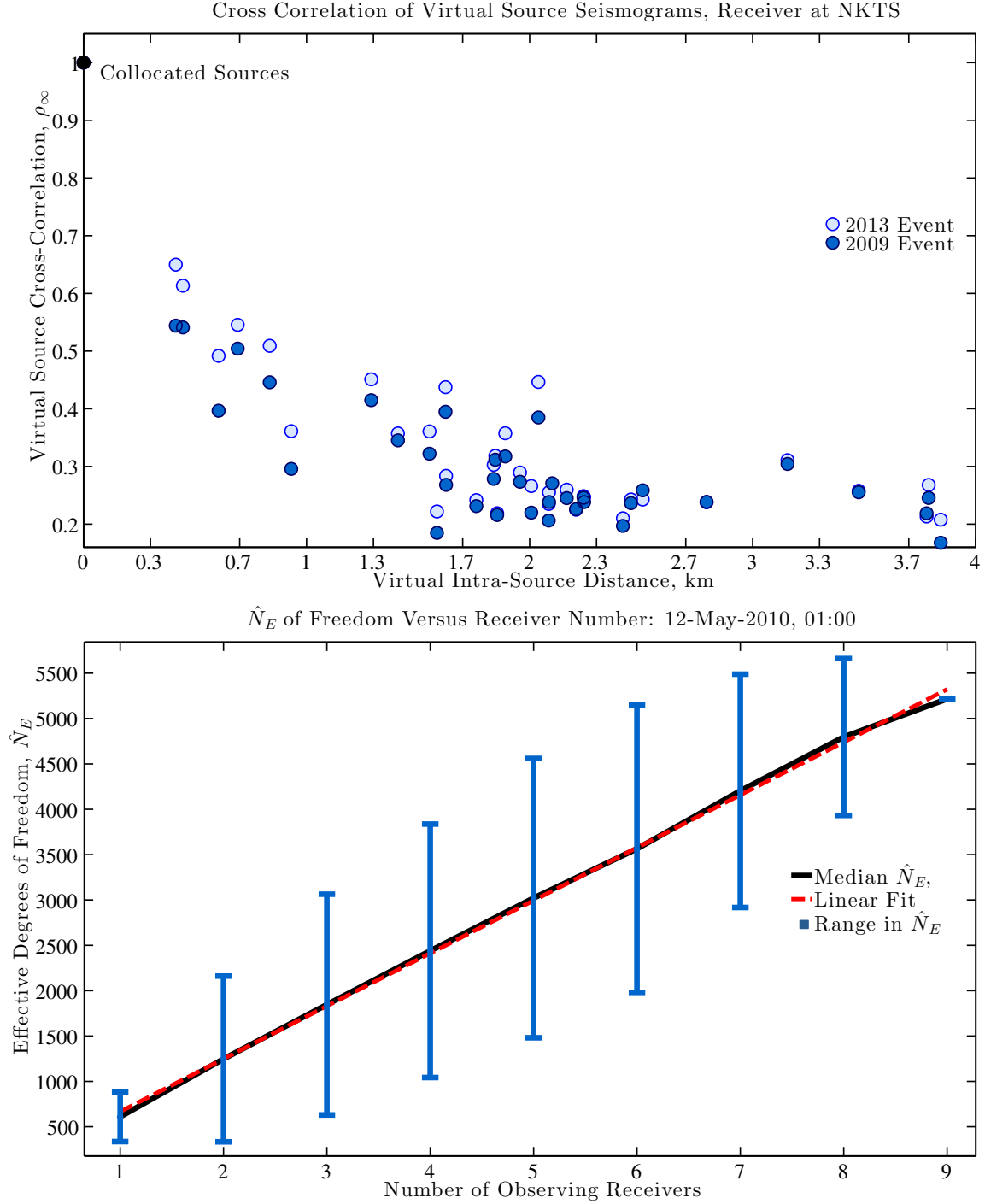


Figure 9: Statistics for virtual correlation detections, using source-receiver reciprocity. **Top:** Correlation values computed by processing a “template” waveform recorded by one element at USRK to detect “target” waveforms recorded at other elements using both 2009 and 2013 test waveforms. Source-receiver reciprocity indicates these coefficients are identical to what would be measured by a single receiver located at the NKTS, when comparing waveforms produced by explosions located at the elements of USRK. **Bottom:** Parameter estimates for \hat{N}_E as a function of recording receivers on DOY 132, 2010. The blue bars illustrate the total range in \hat{N}_E over all combinations of USRK receivers. The black curve indicates the mean value among these bars, and the red curve is the best linear fit. This predictable relationship suggests that density function parameterization for a single virtual receiver at the NKTS can be extrapolated to nine virtual receivers.

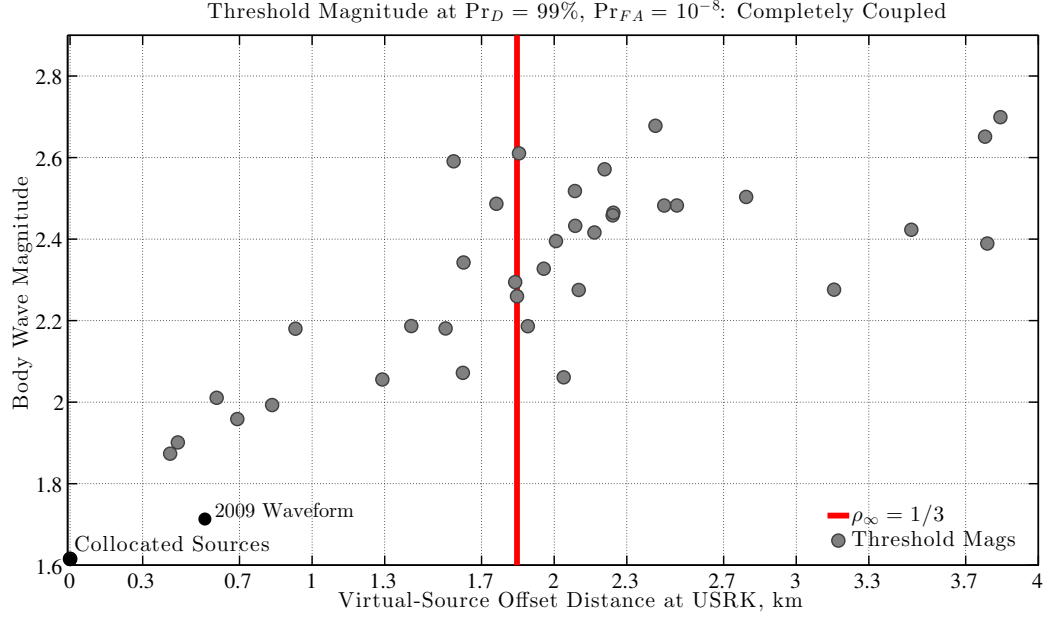


Figure 10: Threshold magnitudes for virtual, explosive sources located 0-4.0 km from a template source at the USRK array, DOY 132, 2010. Values were computed using source-receiver reciprocity between the USRK array at the 2013 announced test location. The gray markers illustrates the magnitude values for which an explosively-triggered waveform has a 0.99 detection probability of being detected using virtual template waveforms (Figure 2) and revised detection thresholds (Figure 3, red markers). Labeled black markers show the threshold value for collocated sources with unit signal correlation, and the threshold value computed from the waveform cross correlation $\hat{\rho}_\infty$ between the 2013 and 2009 announced tests. The red vertical line illustrates the $1/3$ correlation value for reference.

References

- [1] R. R. Blandford. An automatic event detector at the tonto forest seismic observatory. *GEO-PHYSICS GEOPHYSICS*, 39(5):633–643, 1974. ID: 4641584412.
- [2] David Bowers, Peter D Marshall, and Alan Douglas. The level of deterrence provided by data from the spits seismometer array to possible violations of the comprehensive test ban in the novaya zemlya region. *Geophysical Journal International*, 146(2):425–438, 2001.
- [3] Joshua D Carmichael. Multi-Channel Correlation Detectors: Accounting for and Reducing Non-Target Detections. Technical Report LA-UR-15-24554, Los Alamos National Laboratory, Los Alamos, NM, Los Alamos National Laboratory, Los Alamos, NM, United States, 2014. LA-UR-15-24554.
- [4] Joshua D. Carmichael and Dale Anderson. A multichannel detector to target screening challenges in support of test ban treaty verification: Demonstration, performance and application. In *Research Monitoring Review (Albuquerque, New Mexico, June, 2014)*, number LA-UR-14-21435. Department of Energy, NNSA, June 2014. Poster Presentation.
- [5] Joshua D. Carmichael, Ian Joughin, Mark D. Behn, Sarah Das, Matt A. King, Laura Stevens, and Dan Lizarralde. Seismicity on the western greenland ice sheet: Surface fracture in the vicinity of active moulins. *Journal of Geophysical Research: Earth Surface*, pages n/a–n/a, 2015. 2014JF003398.
- [6] Joshua D Carmichael, Robert Nemzek, Stephen Arrowsmith, and Kari Sentz. Detecting weak explosions at local distances by fusing multiple geophysical phenomenologies. *Geophysical Journal International*, 2015. Submitted Jan 09, 2015; Manuscript GJI-S-15-0027.
- [7] Joshua D. Carmichael, Erin C. Pettit, Matt Hoffman, Andrew Fountain, and Bernard Hallet. Seismic multiplet response triggered by melt at blood falls, taylor glacier, antarctica. *Journal of Geophysical Research-Earth Surface*, 117:F03004, JUL 10 2012. PT: J; NR: 51; TC: 1; J9: J GEOPHYS RES-EARTH; PG: 16; GA: 974UL; UT: WOS:000306462800001.
- [8] Anders Christoffersson. Statistical models for seismic magnitude. *Physics of the Earth and Planetary Interiors*, 21(2):237–260, 1980.
- [9] K Michael Cleveland and Charles J Ammon. Precise relative earthquake magnitudes from cross correlation. *Bulletin of the Seismological Society of America*, 2015.
- [10] Wo-Young Kim David P. Schaff and Paul G. Richards. Seismological Constraints on Proposed Low-Yield Nuclear Testing in Particular Regions and Time Periods in the Past, with Comments on “Radionuclide Evidence for Low-Yield Nuclear Testing in North Korea in April/May 2011” by Lars-Erik De Geer. *Science and Global Security: The Technical Basis for Arms Control, Disarmament, and Nonproliferation Initiatives*, 20(2-3):155–171, Oct 23 2012.
- [11] Marvin D Denny and Dennis M Goodman. A Case Study of the Seismic Source Function: Salmon and Sterling Reevaluated. *Journal of Geophysical Research: Solid Earth (1978–2012)*, 95(B12):19705–19723, 1990.
- [12] Marvin D Denny and Lane R Johnson. The Explosion Seismic Source Function: Models and Scaling Laws Reviewed. *Explosion Source Phenomenology*, pages 1–24, 1991.

- [13] DA Dodge and WR Walter. Initial global seismic cross-correlation results: Implications for empirical signal detectors. *Bulletin of the Seismological Society of America*, 2015.
- [14] Sean R Ford and William R Walter. International monitoring system correlation detection at the north korean nuclear test site at punggye-ri with insights from the source physics experiment. *Seismological Research Letters*, 2015.
- [15] Steven J. Gibbons and Frode Ringdal. The Detection of Low Magnitude Seismic Events using Array-Based Waveform Correlation. *Geophysical Journal International*, 165(1):149–166, APR 2006. PT: J; TC: 49; UT: WOS:000239689500013.
- [16] Steven J. Gibbons and Frode Ringdal. Seismic Monitoring of the North Korea Nuclear Test Site using a Multichannel Correlation Detector. *IEEE Transactions on Geoscience and Remote Sensing*, 50(5):1897–1909, May 2012. PT: J; NR: 47; TC: 2; J9: IEEE T GEOSCI REMOTE; PN: Part 2; PG: 13; GA: 931GW; UT: WOS:000303205400015.
- [17] Steven J. Gibbons, Frode Ringdal, and Tormod Kvaerna. Ratio-to-moving-average seismograms: a strategy for improving correlation detector performance. *Geophysical Journal International*, 190(1):511–521, JUL 2012. PT: J; NR: 48; TC: 0; J9: GEOPHYS J INT; PG: 11; GA: 956HO; UT: WOS:000305080900037.
- [18] David B. Harris. Characterizing Source Regions with Signal Subspace Methods: Theory and Computational Methods. Technical Report UCID-21848, Lawrence Livermore National Laboratory, December 1989.
- [19] David B. Harris. A Waveform Correlation Method for Identifying Quarry Explosions. *Bulletin of the Seismological Society of America*, 81(6):2395–2418, December 1991.
- [20] David B. Harris. Subspace Detectors: Theory. Technical Report UCRL-TR-222758, Lawrence Livermore National Laboratory, July 2006. ID: 316300514.
- [21] Steven M. Kay. *Fundamentals of Statistical Signal Processing: Detection Theory*. Prentice-Hall Inc., Upper Saddle River, New Jersey, USA, 1st edition, 1998.
- [22] Leon Knopoff and Anthony F Gangi. Seismic Reciprocity. *Geophysics*, 24(4):681–691, 1959.
- [23] Tormod Kværna and Frode Ringdal. Seismic threshold monitoring for continuous assessment of global detection capability. *Bulletin of the Seismological Society of America*, 89(4):946–959, 1999.
- [24] Tormod Kværna and Frode Ringdal. Detection capability of the seismic network of the international monitoring system for the comprehensive nuclear-test-ban treaty. *Bulletin of the Seismological Society of America*, 103(2A):759–772, 2013.
- [25] William Menke. Using waveform similarity to constrain earthquake locations. *Bulletin of the Seismological Society of America*, 89(4):1143–1146, 1999.
- [26] R. E. Reinke, J. A. Leverette, A. A. Martinez, D. W. Murrell, and C. E. Joachim. High explosive decoupling experiments in hard rock. In *90th Annual Meeting of the Seismological Society of America, El Paso, TX*, 22-24 March 1995.

- 592 [27] F. RINGDAL. Estimation of seismic detection thresholds. *Bulletin of the Seismological Society*
593 *of America*, 65(6):1631–1642, 1975. PT: J; NR: 15; TC: 28; J9: B SEISMOL SOC AM; PG:
594 12; GA: BE659; UT: WOS:A1975BE65900007.
- 595 [28] Frode Ringdal and Tormod Kværna. Continuous seismic threshold monitoring. *Geophysical*
596 *Journal International*, 111(3):505–514, 1992.
- 597 [29] Esteban Rougier and Howard J Patton. Seismic source functions from free-field ground mo-
598 tions recorded on spe: implications for source models of small, shallow explosions. *Journal of*
599 *Geophysical Research: Solid Earth*, 2015.
- 600 [30] David Schaff. Improvements to Detection Capability by Cross-Correlating for Similar Events:
601 a Case Study of the 1999 Xiuyan, China, Sequence and Synthetic Sensitivity Tests. *Geophysical*
602 *Journal International*, 180(2):829–846, 2010.
- 603 [31] David P Schaff. Semiempirical Statistics of Correlation-Detector Performance. *Bulletin of the*
604 *Seismological Society of America*, 98(3):1495–1507, 2008.
- 605 [32] David P Schaff and Paul G Richards. Improvements in magnitude precision, using the statis-
606 tics of relative amplitudes measured by cross correlation. *Geophysical Journal International*,
607 197(1):335–350, 2014.
- 608 [33] Louis L. Scharf and Benjamin Friedlander. Matched subspace detectors. *IEEE Transactions*
609 *on Signal Processing*, 42(8):2146–2156, 1994.
- 610 [34] Megan Slinkard, David Schaff, Natalya Mikhailova, Stephen Heck, Christopher Young, and
611 Paul G Richards. Multistation validation of waveform correlation techniques as applied to
612 broad regional monitoring. *Bulletin of the Seismological Society of America*, 104(6):2768–2781,
613 2014.
- 614 [35] Henry Stark and Yongyi Yang. *Vector Space Projections: A Numerical Approach to Signal and*
615 *Image Processing, Neural Nets, and Optics*. Wiley John and Sons, Incorporated, New York,
616 NY, 1998.
- 617 [36] Jeffry L Stevens and G Eli Baker. Seismic wave generation by a nonisotropic explosion source.
618 *Journal of Geophysical Research: Solid Earth (1978–2012)*, 114(B12), 2009.
- 619 [37] Stephen Weichecki-Vergara, Henry L. Gray, and Wayne A Woodward. Statistical Development
620 in Support of CTBT Monitoring. Technical Report DTRA-TR-00-22, Southern Methodist
621 University, August 2001.
- 622 [38] Miao Zhang and Lianxing Wen. High-precision location and yield of north korea’s 2013 nuclear
623 test. *Geophysical Research Letters*, 40(12):2941–2946, 2013.
- 624 [39] Miao Zhang and Lianxing Wen. Seismological Evidence for a Low-Yeld Nuclear Test on 12
625 May 2010 in North Korea. *Seismological Research Letters*, 2014.

A A Statistical Theory of Correlation Detectors: Target and Non-Target Waveforms

Multichannel correlation detectors compare template waveforms recorded from a given reference event with noisy data to identify similarly shaped waveforms using a sample-correlation coefficient, $s(\mathbf{x})$. This coefficient generalizes the correlation between pairs of single-channel waveforms to pairs of multichannel waveforms that represent measurements of seismic velocity recorded by a clock-synchronized, L -element seismic network [18, 19]. We represent an N -sample seismogram of ground motion history $u_k(t)$ recorded on channel k of this network, digitized from time t_0 until time $N \cdot \Delta t$ at interval Δt , as:

$$\mathbf{u}_k = [u_k(t_0), u_k(t_0 + \Delta t), u_k(t_0 + 2 \cdot \Delta t), u_k(t_0 + (N - 1) \cdot \Delta t)]^T \quad (9)$$

where \mathbf{u}_k is expressed equivalently. Similarly, we represent multichannel data using matrices $\mathbf{u} = [\mathbf{u}_1, \mathbf{u}_2, \dots, \mathbf{u}_L]$, where column k contains digitized seismogram \mathbf{u}_k sampled from time t_0 at interval Δt until time $t_0 + N\Delta t$, and rows 1 through $N - 1$ of \mathbf{u} sequentially contain ground motion measured at respective times $t_0, t_0 + \Delta t, \dots, t_0 + N\Delta t$; again, \mathbf{w} is defined equivalently. A correlation detector tests the sample correlation $s(\mathbf{x})$ between a multichannel template waveform \mathbf{u} and commensurate data stream matrix \mathbf{x} against a computed threshold η according to the following decision rule [18, 6, 7, 10]:

$$s(\mathbf{x}) = \frac{\sum_k^L \mathbf{x}_k^T \mathbf{u}_k}{\sqrt{\sum_k^L \mathbf{x}_k^T \mathbf{x}_k \cdot \sum_k^L \mathbf{u}_k^T \mathbf{u}_k}} = \frac{\langle \mathbf{x}, \mathbf{u} \rangle_F}{\|\mathbf{u}\|_F \|\mathbf{x}\|_F} \underset{\mathcal{H}_0}{\overset{\mathcal{H}_1}{\gtrless}} \eta. \quad (10)$$

The term $\langle \mathbf{x}, \mathbf{u} \rangle_F = \text{tr}(\mathbf{x}^T \mathbf{u})$ is the Frobenius inner product, which generalizes dot products to matrices. Similarly, the term $\|\mathbf{x}\|_F = \sqrt{\text{tr}(\mathbf{x}^T \mathbf{x})}$ is the Frobenius norm, and generalizes vector norms to matrices. The hypothesis \mathcal{H}_0 above the conditional inequality in Equation 10 signifies that \mathbf{x} consists of Gaussian noise ($\mathbf{x} = \mathbf{n}$) when $s(\mathbf{x}) < \eta$; the hypothesis \mathcal{H}_1 signifies that \mathbf{x} consists of a scaled-copy $\mathbf{w} = A\mathbf{u}$ of the template waveform \mathbf{u} buried in Gaussian noise ($\mathbf{x} = A\mathbf{u} + \mathbf{n}$) if $s(\mathbf{x}) > \eta$. Under \mathcal{H}_1 , the maximum likelihood estimate for the (unknown) scale amplitude A is [6]:

$$\hat{A} = \frac{\langle \mathbf{x}, \mathbf{u} \rangle_F}{\|\mathbf{u}\|_F^2} \quad (11)$$

In contrast to these conventional data models, noisy non-target waveforms originating from background seismicity may also be recorded and mis-detected. Such false-detections occur if a signal within the data stream is sufficiently coherent with the template waveform that the correlation $s(\mathbf{x})$ exceeds the prescribed threshold for event declaration (η in Equation 10). In practice, this threshold so high that white noise has a very low chance of generating false detections, and therefore spuriously high correlation values are usually induced by nearly monochromatic noise or non-target seismicity. Alternatively, target waveforms that are (nearly) collocated with the template source may still generate lower-than-predicted cross-correlation (< 1) if the underlying signals exhibit incoherence with

the template signal due to differences in radiation pattern [13], corner frequency [14], or damage production [29]. In the general case that the wavefield includes Gaussian noise-contaminated non-target and target signals, the correlation statistic $s(\mathbf{x})$ follows a four-scalar parameter probability density function known as the doubly-noncentral Beta distribution [20, 6]. The first of these four parameters is fixed at one-half. The second is proportional to the effective degrees of freedom N_E in the data and quantifies the temporal correlation of the contaminating noise [37, 6, 4]. The other two are known as noncentrality parameters. The first noncentrality parameter λ is proportional to the multichannel cross-correlation ρ_∞ of the template and underlying target signal \mathbf{w} in the data stream \mathbf{x} :

$$\begin{aligned}\rho_\infty &= \frac{\langle \mathbf{w}, \mathbf{u} \rangle_F}{\|\mathbf{u}\|_F \|\mathbf{w}\|_F} \\ &= \sqrt{\text{tr} \left(\frac{\mathbf{w}^T \hat{\mathbf{u}} \hat{\mathbf{u}}^T \mathbf{w}}{\|\mathbf{w}\|^2} \right)}\end{aligned}\quad (12)$$

where $\hat{\mathbf{u}}$ is the normalized multichannel template waveform and we assume the target and template waveforms are imperfectly correlated. The second noncentrality parameter λ^\perp is proportional to the SNR of non-target waveforms in \mathbf{x} and is zero when a true scaled copy of the template waveform is present. In the present context, the first of noncentrality parameter is defined by:

$$\begin{aligned}\lambda &= \text{tr} \left(\frac{\mathbf{w}^T \hat{\mathbf{u}} \hat{\mathbf{u}}^T \mathbf{w}}{\sigma_0^2} \right) = \rho_\infty^2 \frac{\|\mathbf{w}\|^2}{\sigma_0^2} \\ &= N \cdot \rho_\infty^2 \text{SNR}(\mathbf{x}).\end{aligned}\quad (13)$$

This parameter is additionally related to the maximum likelihood estimate for the waveform amplitude in target-signal present case (\mathcal{H}_1), in which case:

$$\hat{A}^2 = \frac{\lambda \cdot \sigma^2}{\|\mathbf{u}\|_F^2} \quad (14)$$

This relationship between the waveform amplitude estimate and λ is important for estimating threshold magnitudes; we will implement it later.

The second noncentrality parameter is defined by:

$$\begin{aligned}\lambda^\perp &= \text{tr} \left(\frac{\mathbf{w}^T (\mathbf{I} - \hat{\mathbf{u}} \hat{\mathbf{u}}^T) \mathbf{w}}{\sigma_0^2} \right) = (1 - \rho_\infty^2) \frac{\|\mathbf{w}\|^2}{\sigma_0^2} \\ &= N \cdot (1 - \rho_\infty^2) \text{SNR}(\mathbf{x}),\end{aligned}\quad (15)$$

where \mathbf{I} is an $L \times L$ identity matrix. With these parameters defined, the signal-present probability distribution function for the correlation statistic is:

$$f_1(s(\mathbf{x}); \mathcal{H}_1) = \text{B} \left(s^2(\mathbf{x}); \frac{1}{2}, \frac{1}{2}(N_E - 1), \lambda, \lambda^\perp \right) + \text{B} \left(-s^2(\mathbf{x}); \frac{1}{2}, \frac{1}{2}(N_E - 1), \lambda, \lambda^\perp \right) \quad (16)$$

where $B(t, N_1, N_2, \alpha, \beta)$ is the doubly noncentral Beta distribution function. It is evaluated at t , has N_1 and N_2 degrees of freedom, and noncentrality parameters α and β . In the current application, the noncentrality parameters are constrained by Equations 13 and 15 according to a signal correlation-dependent proportionality constant:

$$\lambda^\perp = \left(\frac{1 - \rho_\infty^2}{\rho_\infty^2} \right) \lambda \quad (17)$$

Under this constraint, the probability of detecting any signal characterized by λ and λ^\perp is equal to the right-tail probability of $f_1(s(\mathbf{x}); \mathcal{H}_1)$ and is computed by integrating this density function from a threshold η (defined in Equation 10), to one. With full parametrization, this includes cases where the data contain only noise ($\lambda = 0, \lambda^\perp = 0$), noisy non-target signals ($\lambda = 0, \lambda^\perp > 0$), noisy target signals ($\lambda > 0, \lambda^\perp = 0$), and a superposition of noisy non-target and target signals ($\lambda > 0, \lambda^\perp > 0$). The signal absent, or “null” distribution $f_0(s(\mathbf{x}); \mathcal{H}_0)$ is equivalent to $f_1(s(\mathbf{x}); \mathcal{H}_1)$ with $\lambda = \lambda^\perp = 0$. We detect template-shaped waveforms in noise using Equation 10 at a threshold η established by $f_0(s(\mathbf{x}); \mathcal{H}_0)$ at an acceptable false alarm probability (10^{-8}) using the Neyman Pearson criteria [21]:

$$10^{-8} = \Pr_{FA} = \int_\eta^1 f_0(s; \mathcal{H}_0) ds \quad (18)$$

We explicitly estimate the detection threshold η as $\hat{\eta}$ using Equation 18, acknowledging that $f_0(s; \mathcal{H}_0)$ is not perfectly known. We compute the associated probability of detecting a target waveform that produces a correlation statistic parametrized by λ and λ^\perp by integrating $f_1(s; \mathcal{H}_1)$ over the acceptance region established by \Pr_{FA} :

$$\begin{aligned} \Pr_D &= \int_\eta^1 f_1(s; \mathcal{H}_1) ds, \\ &\triangleq \Pr_D(\eta, \lambda, \lambda^\perp, N_E). \end{aligned} \quad (19)$$

A.1 Effective Degrees of Freedom

Both density functions $f_k(s; \mathcal{H}_k)$ ($k = 0, 1$) are parametrized by the effective number of independent data stream samples N_E , which theoretically equate to twice the time-bandwidth product $2BT$ of \mathbf{u} . Real data often show that $N_E \ll 2BT$, however. This occurs both naturally and through processing operations like bandpass filtering, which replace each sample with itself plus a weighted sum of its neighbors and thereby introduce intra-sample statistical dependence. Such correlation structure generally requires a non-diagonal covariance matrix $\mathbf{\Sigma} \neq \sigma^2 \mathbf{I}$ for \mathbf{x} . However, we observed that we could account for the structure in our data using a scalar N_E that parametrizes each probability density function and represents the effective number of statistically independent samples in \mathbf{x} . We therefore implemented this empirical estimator for N_E , denoted \hat{N}_E , to continuously update parameterizations for $f_0(s; \mathcal{H}_0)$ (see [37, Section 2.4]). This estimator computes the sample correlation between the multichannel template waveform \mathbf{u} and several hundred psuedo-random, commensurate data vectors drawn from non-intersecting segments of pre-processed, signal sparse data within \mathbf{x} . We compute the sample variance $\hat{\sigma}_S^2$ of the resultant correlation time series using

709 99.9% of the data by excluding 0.01% of the extreme left and right tails of its histogram. This
 710 provides the needed statistic to estimate N_E , given by:

$$\hat{N}_E = 1 + \frac{1}{\hat{\sigma}_S^2}, \quad (20)$$

711 and thereby estimate $f_k(s; \mathcal{H}_k)$ ($k = 0, 1$) and $\hat{\eta}$.

712 A.2 Verification of the Signal-Present Density Function

713 The density function in Equation 16 differs from what has been derived by Weichecki-Vergara and
 714 others [37]. In that case, the authors assumed that template and target waveforms had uniform
 715 correlation over the duration of their respective signals. We evaluated this assumption using 180
 716 second records from 2009 and 2013 announced test waveforms that were recorded at USRK. We
 717 thereby aligned both multichannel waveforms at the peak P_n correlation delay time, and computed
 718 a one-second width sliding window correlation coefficient over the aligned signals (Figure 11). We
 719 implemented this localized correlation sample by sample by computing a modified, sliding window
 720 correlogram. At a given time lag, this local correlation computes a localized correlation coefficient:

$$s_B(\mathbf{x}) = \frac{\langle \mathbf{u}_1 \cdot \mathbf{u}_2, \mathbf{B} \rangle_F}{\|\mathbf{u}_1 \cdot \mathbf{B}\|_F \cdot \|\mathbf{u}_2 \cdot \mathbf{B}\|_F}, \quad (21)$$

722 where \mathbf{B} is a one second width (boxcar) window that localizes the action of the correlation com-
 723 putation, \mathbf{u}_1 is the 2013 multichannel waveform, and \mathbf{u}_2 is the 2009 multichannel waveform. We
 724 implemented Equation 21 in the frequency domain as conventionally done with cross correlation.
 725 This analysis produced a time series that showed certain portions of the waveforms were substan-
 726 tially more correlated than others, with portions of P_n and P_g exhibiting greater waveform similarity
 727 relative to similar duration portions of L_g . If the underlying signals were instead uniformly corre-
 728 lated, we would expect the correlation trace to vary about a mean value.

729 Having established that repeating explosions are not uniformly correlated, we followed Schaff [31]
 730 and performed a semi-empirical detection routine using a transient (11 sec length) template wave-
 731 form recorded from an event local to USRK to validate our signal-present density function in
 732 Equation 16. While this template differs from what we used in Section 4.1, it allowed us to sam-
 733 ple more data per day and more quickly estimate the data's effective degrees of freedom, N_E to
 734 . We first pre-processed this template with a 1.5-7.5 Hz bandpass filter and tapered it to reduce
 735 any spectral leakage. Second, we embedded the template $\sim 5 \cdot 10^3$ times into identically filtered,
 736 recorded background noise and then processed this resultant data with our template. This pro-
 737 duced an set of $\sim 5 \cdot 10^3$ correlation values that we then binned into a histogram for comparison
 738 with our parameterized density function (Equation 16). Figure 12 illustrates this histogram plotted
 739 with $f_1(s(\mathbf{x}); \mathcal{H}_1)$. The density curve is parameterized by the expected value for both λ and λ^\perp
 740 (Equations 13 and 15), as computed from the false detections in Figures 3 and 6.

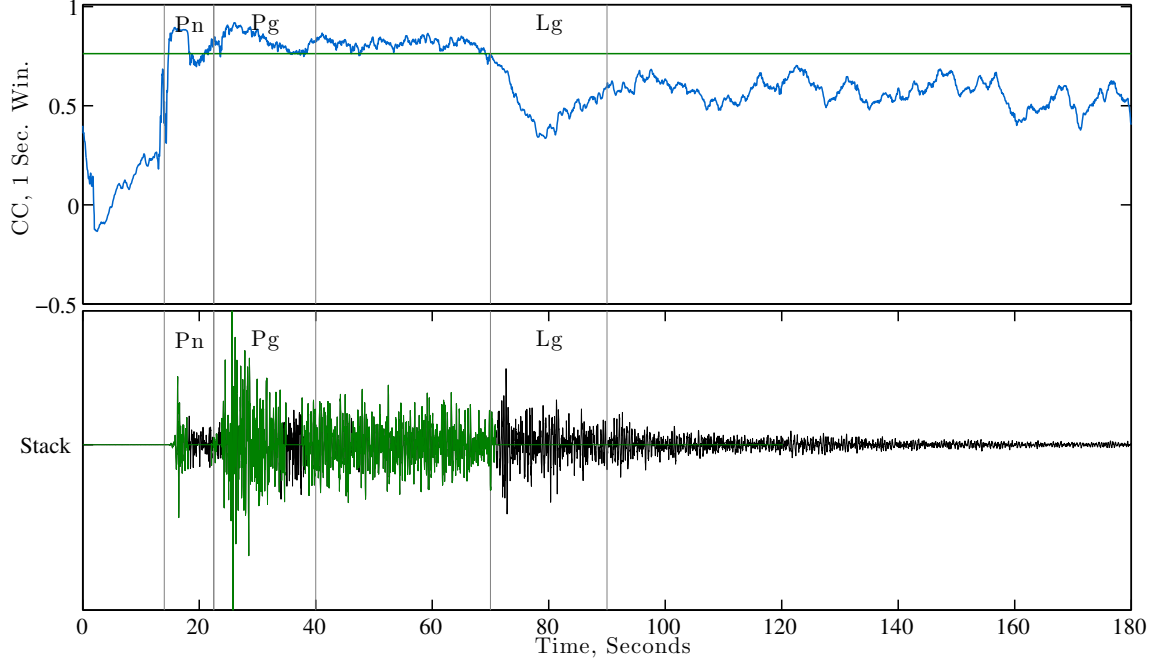


Figure 11: Localized correlation between the pre-aligned multichannel waveforms recording the 2009 and 2013 announced NKTS tests. **Top:** The local sample correlation between the pre-aligned waveforms in a one ses sliding window using Equation 21. The green line shows an arbitrary $\frac{1}{\sqrt{2}}$ correlation value. **Bottom:** The intra-channel stack of the 2013 test waveforms. The green portions of the waveforms show where the data are correlated above $\frac{1}{\sqrt{2}}$ and indicate that the two signals are not uniformly correlated across their duration.

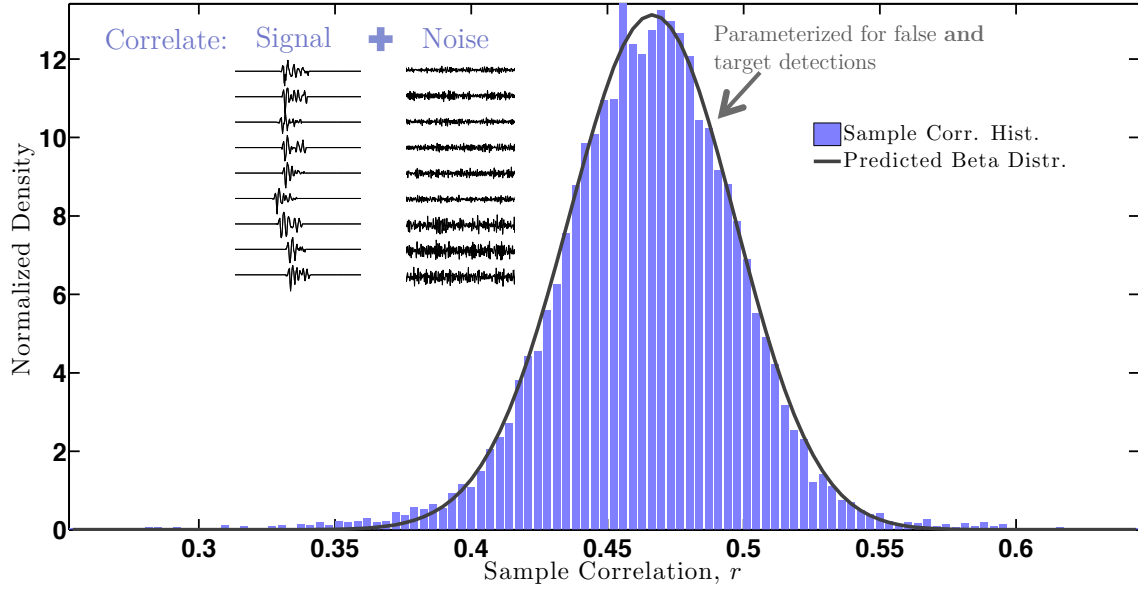


Figure 12: The empirical probability density function (histogram, purple) for the correlation statistic obtained by processing an 11 sec template waveform (pictured) against noisy data streams embedded with a scaled version of the template. Data were selected from DOY 114 to DOY 134 and waveforms that included STA/LTA detections were excluded to avoid sampling from different distributions. The dark curve illustrates the hypothesized density function $f_1(s(\mathbf{x}); \mathcal{H}_1)$ parameterized by λ and the expected value for λ^\perp , as computed from background seismicity (Figure 3). (Figure adapted from Carmichael and Anderson [4]).

B Relative Magnitudes of Collocated, Similar Explosions

We first define relative magnitudes of collocated explosions in the noise-free case, and then derive an estimator applicable to noise-dominated cases. We specifically consider two collocated explosions that generate multichannel seismic waveforms $\mathbf{u}(t)$ and $\mathbf{w}(t)$ with amplitudes A_1 and A_0 , measured at period T by the same network of L clock-synchronized receivers. We further assume that waveforms \mathbf{u} and \mathbf{w} are triggered by sources that share a common radiation pattern and are therefore proportional in amplitude through a scaling constant $A = \frac{A_0}{A_1}$. A typical magnitude scale relates the log-ratio of these two (true) waveform amplitudes at their identical observation distance r through equations of the form:

$$\begin{aligned} m_0 &= \log_{10} \left(\frac{A_0}{T} \right) - m_C(r, r_C) \\ m_1 &= \log_{10} \left(\frac{A_1}{T} \right) - m_C(r, r_C) \end{aligned} \quad (22)$$

In Equation 22, m_l is the true magnitude of event l ($l = 0, 1$) and m_C is a calibration magnitude that depends on a calibration distance r_C and other magnitude-independent parameters (not shown). For small aperture arrays, r represents the common source-to-array center distance and the amplitudes A_l are averaged over the common array aperture. The true magnitude difference between these events is then proportional to the log-ratio of their squared amplitudes:

$$\begin{aligned} \Delta m &= m_0 - m_1 \\ &= \frac{1}{2} \log_{10} \left(\frac{A_0^2}{A_1^2} \right) \\ &= \frac{1}{2} \log_{10} (A^2), \end{aligned} \quad (23)$$

where terms $m_C(r, r_C)$ in Equation 22 arithmetically cancel. Because the two explosive sources producing waveforms \mathbf{w} and \mathbf{u} share a common radiation pattern, their relative magnitudes are also expressible using the ratio of their signal energies, since $A^2 = \frac{\|\mathbf{w}\|_F^2}{\|\mathbf{u}\|_F^2}$, where the term $\|\mathbf{w}\|_F = \sqrt{\text{tr}(\mathbf{w}^T \mathbf{w})}$ is the Frobenius norm, and generalizes vector norms to matrices.

For real observations contaminated by seismic and digital noise, neither true waveforms or magnitudes are directly observable and Equation 23 only represents an infinite signal-to-noise ratio (SNR) estimate of relative magnitudes. A realistic, noisy data record \mathbf{x} that contains waveform \mathbf{w} that is proportional in amplitude to \mathbf{u} is represented as:

$$\mathbf{x} = A\mathbf{u} + \mathbf{n}, \quad (24)$$

where \mathbf{n} is (zero-mean) contaminating noise. Under these noisy conditions, Schaff and Richards [32] derived an estimator for the observed magnitude $\Delta \hat{m}_O$ of a detected target event relative to

767 that of reference event that is equivalent to:

$$\Delta\hat{m}_O = \frac{1}{2} \log_{10} \left(\frac{\|\mathbf{x}\|_F^2}{\|\mathbf{u}\|_F^2} \right), \quad (25)$$

768 where we assume that the SNR of \mathbf{u} is much larger than the SNR of \mathbf{x} ($\text{SNR}(\mathbf{u}) \gg \text{SNR}(\mathbf{x})$). This
 769 estimate (Equation 25) is unbiased by sample correlation, but is biased by noise. In the limiting
 770 case that waveform \mathbf{u} has zero SNR, Equation 25 becomes:

$$\lim_{A \rightarrow 0} \Delta\hat{m}_O = \frac{1}{2} \log_{10} \left(\frac{\|\mathbf{n}\|_F^2}{\|\mathbf{u}\|_F^2} \right) \quad (26)$$

771 where \mathbf{n} is the measured noise from Equation 24. Without bias, the actual relative magnitude in the
 772 absence of signal must physically approach $\Delta m = -\infty$. We now quantify this bias by considering
 773 the expected value of the logarithm's argument. First, we expand the data energy ratio in Equation
 774 25, assuming common radiation patterns and waveform scaling:

$$\frac{\|\mathbf{x}\|_F^2}{\|\mathbf{u}\|_F^2} = A^2 + \frac{2A \cdot \langle \mathbf{n}, \mathbf{u} \rangle_F}{\|\mathbf{u}\|_F^2} + \frac{\|\mathbf{n}\|_F^2}{\|\mathbf{u}\|_F^2}. \quad (27)$$

775 The term $\langle \mathbf{x}, \mathbf{u} \rangle_F = \text{tr}(\mathbf{x}^T \mathbf{u})$ is the Frobenius inner product, and generalizes dot products to
 776 matrices. If σ_0^2 is the (zero mean) noise variance, the expected value $\mathbb{E}\{\bullet\}$ of this quotient is:

777

$$\begin{aligned} \mathbb{E} \left\{ \frac{\|\mathbf{x}\|_F^2}{\|\mathbf{u}\|_F^2} \right\} &= \mathbb{E} \{ A^2 \} + \mathbb{E} \left\{ \frac{2A \cdot \langle \mathbf{n}, \mathbf{u} \rangle_F}{\|\mathbf{u}\|_F^2} \right\} + \mathbb{E} \left\{ \frac{\|\mathbf{n}\|_F^2}{\|\mathbf{u}\|_F^2} \right\} \\ &= A^2 + \frac{\sigma_0^2 N_E}{\|\mathbf{u}\|_F^2} \end{aligned} \quad (28)$$

778 The term $\sqrt{\frac{\sigma_0^2 N_E}{\|\mathbf{u}\|_F^2}}$ represents the source of noise bias. In practice, both the noise sample variance σ_0^2
 779 and the waveform amplitude are unknown. First, we estimate $\hat{\sigma}_0^2$ by excluding background signals
 780 identified with a power detector, as discussed in Section 4.1. To estimate A^2 values, we relate
 781 its maximum likelihood estimate to the correlation density function's noncentrality parameter λ
 782 (Equation 14). We thereby propose the following estimator for Δm by combining Equations 28
 783 and 14:

$$\Delta\hat{m} = \frac{1}{2} \log_{10} \left(\left| \frac{\lambda \cdot \hat{\sigma}_0^2}{\|\mathbf{u}\|_F^2} - \frac{\hat{\sigma}_0^2 N_E}{\|\mathbf{u}\|_F^2} \right| \right), \quad (29)$$

784 where the absolute value operator in Equation 29 prevents the relative magnitude from becoming
 785 complex. Extension to non collocated sources is discussed in Section 4.2, Equation 8.